J Nondestruct Eval (2017) 36:57
DOI 10.1007/s10921-017-0435-3

Effect of Defect Size on Subsurface Defect Detectability and Defect Depth Estimation for Concrete Structures by Infrared Thermography

Shuhei Hiasa[1,2] · **Recep Birgul**[1,3] · **F. Necati Catbas**[1,4]

Received: 13 February 2017 / Accepted: 24 July 2017 / Published online: 31 July 2017

Abstract This study aims to reveal the effect and correlation of delamination size and defect shape for using infrared thermography (IRT) through FE modeling to enhance the reliability and applicability of IRT for effective structural inspections. Regarding the effect of delamination size, it is observed that the temperature difference between sound and delaminated area (ΔT) increases as the size of delamination increases; however, ΔT converges to a certain value when the area is 40×40 cm and the thickness is 1 cm. As for the shape of delamination, it can be assumed that if the aspect ratio which is the ratio of the length of the shorter side to the longer side of the delamination is more than 25%, ΔT of any delaminations converges to ΔT of the same area of a square/circular-shaped delamination. Furthermore, if the aspect ratio is 25% or smaller, ΔT becomes smaller than the ΔT of the same area of a square/circular-shaped delamination, and it is getting smaller as the ratio becomes smaller. Furthermore, this study attempts to estimate depths of delaminations by using IRT data. Based on the correlation between the size of delamination and the depth from the concrete surface in regard to ΔT, it was assumed that it was possible to estimate the depth of delamination by comparing ΔT from IRT data to ΔT at several depths obtained from FE model simulations. Through the investigation using IRT data from real bridge deck scanning, this study concluded that this estimation method worked properly to provide delamination depth information by incorporating IRT with FE modeling.

Keywords Infrared thermography · Non-destructive evaluation · Bridge inspection · FE modeling · Effect of delamination size · Estimation of delamination depth

1 Introduction

Infrared thermography (IRT) is a non-destructive evaluation (NDE) method, and has been developed to detect invisible subsurface defects including delaminations and voids in concrete structures with reasonable accuracy; it also helps avoid the time and expense of gaining immediate access to the concrete surface in order to conduct traditional sounding tests such as hammer sounding and/or chain drag [1]. IRT can be classified into two methods; passive and active IRT. Passive IRT is applied under natural circumstances while active IRT is conducted with thermal excitation; i.e., the main heat sources are solar radiation and ambient temperature for passive IRT, and heat generators for active IRT [2,3]. The principle of passive IRT is as follows: solar loading heats up the concrete surface. If there is a subsurface defect, air fills that area and acts as a thermal insulator by preventing heat from penetrating to the concrete beneath the delamination due to the different thermal conductivities between air (0.0241 W/m °C) and concrete (1.6 W/m °C). Thus, the

✉ F. Necati Catbas
catbas@ucf.edu

Shuhei Hiasa
hiasa615@Knights.ucf.edu; s.hiasa.aa@w-nexco.co.jp

Recep Birgul
rbirgul@gmail.com

1 Department of Civil, Environmental, and Construction Engineering, University of Central Florida, Pegasus Drive, Suite 211, Orlando, FL 12800, USA

2 West Nippon Expressway Company Limited (NEXCO-West), Dojima Avanza 19F, 1-6-20 Dojima, Kita-ku, Osaka 530-0003, Japan

3 Department of Civil Engineering, Mugla Sitki Kocman University, Mugla, Turkey

4 Department of Civil and Environmental Engineering, Bogazici University, Istanbul, Turkey

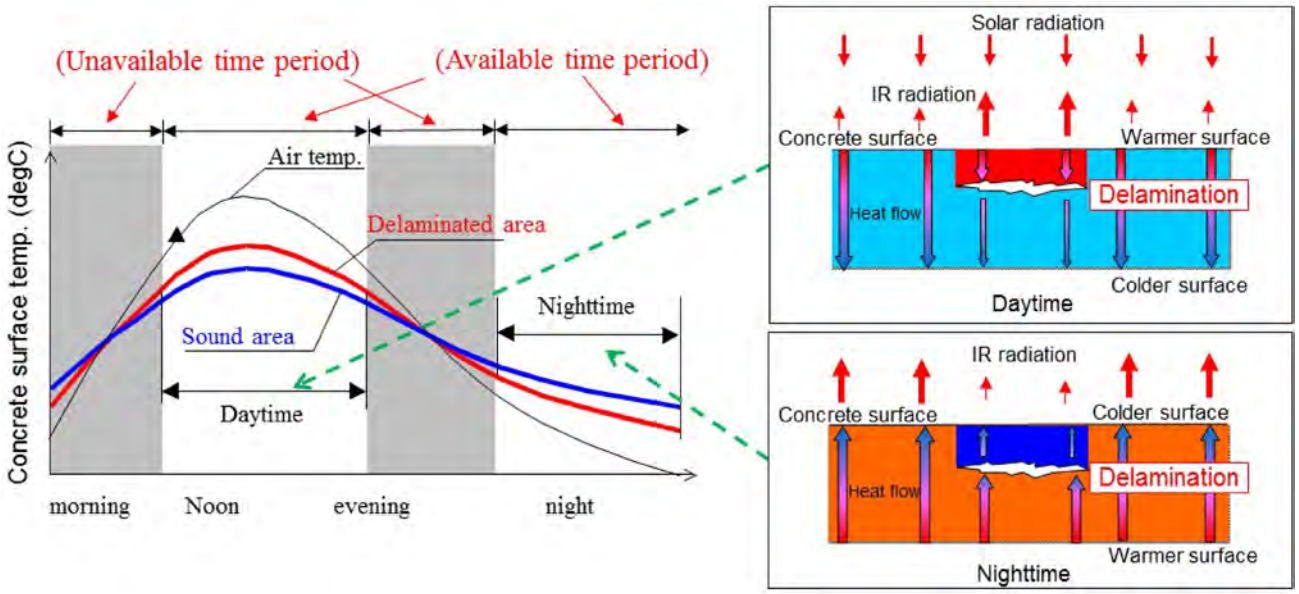

Fig. 1 Assumed applicable time periods of IRT (*left*) and images of heat transfer (*right*)

concrete above the delamination becomes warmer than the surroundings during the daytime (heating cycle) since that area conducts heat faster from the surface to the delamination than the surroundings from the surface to the undersurface, while that same area cools down faster than the surroundings during the nighttime (cooling cycle) as depicted in Fig. 1 [4]. IRT detects subsurface defects by capturing those temperature differences (ΔT) of a concrete surface by reading the emitted infrared (IR) radiation from the concrete surface and converting it to a temperature [5]. Under passive IRT conditions, it is not always possible to detect the delamination of concrete since there should be interchange periods between heating and cooling cycles and those time periods are unavailable for passive IRT as shown in Fig. 1. Moreover, sometimes it becomes difficult to detect delaminations from only the color variation of IRT images since the concrete structure itself tends to have a temperature gradient depending on the location and orientation with respect to the sun. As Washer et al. [6] argued, if the temperature span for IR images is setup too high or too low, it appears as if there is no anomaly in the IR image even though there are some defects. Therefore, proper temperature span adjustment of IR images is required for passive IRT, although this can be done during the post processing. On the other hand, the use of active IRT technique is never affected by data collection time. However, the limitation of active IRT is that it requires homogeneous heating of the concrete surface ranging from several minutes to a couple of hours; shallower delaminations located at 1–4.5 cm deep can be detected with shorter heating time, e.g. 5–10 min, although the defect indications become clearer with an increase in the heating time up to 25–30 min [7,8]. On the other hand, deeper delaminations at a depth of around 10 cm require 1–2 h of heating [8]. In order to detect deeper delaminations, a much longer duration for heating-up the surface is indispensable. Furthermore, active IRT requires installation of heat sources. Therefore, active IRT is impractical for concrete bridge deck inspections due to the challenges of heating huge civil structures uniformly over a period of time as mentioned in [8]. Especially in the US, passive IRT should be chosen for effective and efficient bridge inspections since the inspection area is too enormous (e.g. highway bridges: 93%–346 km^2 out of 371 km^2 in bridge deck area as of 2016 [9]) for active IRT. Although there are some inherent limitations, NDE techniques with passive IRT still offer advantages over conventional inspection techniques such as hammer sounding and chain drag if it is utilized under proper conditions [10–12].

As many researchers suggest, IRT is a suitable approach for inspection of civil infrastructures since it is a non-contact method and IR images can instantly portray a wide range of concrete structures at one time [13–16]. Especially for bridge decks, IRT can scan decks at highway speeds without lane closures. As to bride deck scanning, ground penetrating radar (GPR) with an air-coupled system can also provide high-speed scanning; however, it requires GPR scanning several times to collect data for one lane width using a single-channel system [17]. Even though multiple-antenna systems can provide entire lane scanning in one pass, a single-channel system seems to be used widely due to budgetary constraints for multiple-antenna systems [17]. In addition to bridge deck inspection, IRT can be applied at a much farther distance from the objects; thus, IRT has a big advantage for bridge inspections over other NDE methods because the underside of decks, girders, piers, railings and other components as

well as decks are quite large to inspect with methods that require access and contact to the concrete surface. Therefore, IRT can be the fastest and easiest NDE methodology in terms of data collection compared to the other NDE methods. Although there is a good amount of research on IRT up to the present, each study was conducted under different conditions, making it difficult to draw generalized conclusions. Thus, there are still several uncertainties regarding the accuracy and reliability of IRT for application to bridge inspection when compared to a sounding test [12].

The objective of this study is investigating the effect of delamination size regarding the correlation between the size of delamination and detectability of IRT to enhance the reliability and applicability of IRT for effective bridge inspections. An investigation of the effect of delamination size found that area of delamination strongly affects the detectability of IRT [18]. However, the influence of delamination size is still not clarified entirely. In this study, the effects of area, thickness, shape and depth of delamination on subsurface defect detectability of IRT are explored by finite element (FE) modeling. It is also important to understand whether or not the effect is getting bigger as the area/thickness of delamination is getting bigger, or if it converges to a certain value at a certain area/thickness of delamination. The understanding of characteristics and impacts of defect size on IRT would lead to improvement of IRT data interpretation since the implementation of the methodology has not been fully established on real life structures. Furthermore, estimating the depths of delaminations has been considered one of the limitations of IRT, so if it becomes possible to overcome this limitation based on the understanding, there would be a great improvement in IRT's usefulness for concrete structure inspections. According to Vavilov [19], an evaluation method to estimate the depth and thickness of the delamination was formulated based on the experimental maximum thermal contrast, defect size, sample thickness and heating time under active IRT condition. However, passive IRT is a time dependent methodology as mentioned in the principal, and another approach is desirable for estimating the depth of delamination. Thus, this study also investigates the possibility to estimate the depth of the delamination using passive IRT for an in-service bridge as a case study.

2 Important Factors of IRT for Delamination Detection

Through literature reviews, several factors that might affect the performance of IRT can be excerpted such as data collection time, data collection speed, IR camera specifications, delamination size, and delamination depth. Regarding data collection time, there are contradictory reports regarding appropriate time frames for IRT measurements. Washer et al. [20] recommended daytime measurements 5–9 h after sunrise to detect subsurface delamination; 5–7 h after sunrise for 5.1 cm (2 in.) deep delamination, and 7–8 h after sunrise for 7.6 cm (3 in.) deep delamination for the solar loading part. They also recommended 5 h and 40 min after sunrise for 2.5-cm deep targets and more than 9 h after sunrise for a target at a depth of 12.7 cm (4 in.) [21]. On the other hand, others assert contrary conclusions; Gucunski et al. [22] mentioned a thermal image recorded 40 min after sunrise yielded a much clearer image than another recorded around noon. Additionally, some of the responses of delaminations were described as weaker in IR images, i.e., ΔT became smaller and IR images showed very low-temperature variations, as the time progresses from noon to 3 p.m. while those were clearly indicated during the time period from 10 a.m. to noon [23]. Moreover, Kee et al. [24] also concluded that no indication was found from the IR image taken 3 h and 45 min after sunrise (with the shallowest delamination located at 6.4 cm (2.5 in.) depth) while the best results were achieved using the cooling cycle, 45 min after sunrise, in which even 15.2 cm (6 in.) deep delaminations could be detected. Furthermore, Watase et al. [25] proposed a favorable time for inspection depending on the parts of the bridge; noon time for the deck top, and midnight for the deck soffit. Through several experiments and FE modeling, Hiasa [10] concluded that the preferable time period to apply IRT for concrete bridge deck inspection is during the nighttime cooling effect in order to reduce the possibility of misdetection.

In terms of data collection speed, Hiasa et al. [11,12] conducted comparative studies with three different types of infrared (IR) cameras at a normal driving speed, from 48 to 64 km/h (30–40 mph). It was found that if shorter integration time devices, which are typically equipped on cooled type cameras, are used for high-speed scanning of concrete bridge decks, they are not affected by data collection speeds. It should be noted that even though less than 16 km/h (10 mph) is recommended for data collection speed according to the ASTM standard [26], high-speed scanning by IRT with a cooled type IR camera performed at a similar or better level of accuracy compared to other NDE methods such as impact echo (IE), GPR and chain drag [11]. Therefore, the use of appropriate IR cameras attached to vehicles makes it is possible to collect reliable data rapidly without the need for lane closures, thereby eliminating the need for sounding inspection or other NDE techniques including robotics-assisted system, which mostly requires lane closures. Thus, IRT becomes a more practical and faster method of conducting bridge deck inspections than other NDE technologies.

In regards to camera specifications, a lot of research on IRT has been conducted with one IR camera despite literature that points out the effect of IR camera specifications on

detectability; mostly uncooled cameras have been utilized by the research due to economic efficiency. As mentioned above, the integration time of IR cameras is the most critical factor for high-speed application. In terms of the effect of pixel resolution, lower pixel resolution, 320×240 pixels, caused much lower performance when the camera was attached on a vehicle to take images of one lane width of a roadway, and this result indicates that a pixel resolution of more than 640×480 pixels is preferable for efficient bridge deck inspections [11,12]. Even though IR cameras with lower resolution can take better quality images if they are used at a closer distance, the area that can be taken at one time also becomes much smaller. Thus, data collection must be implemented three or four times more than higher resolution cameras, or three or four cameras should be used at the same time to collect data of one complete lane [12]. Furthermore, the effect of spectral range is also discussed by some researchers. Hashimoto and Akashi [27] reported that IR cameras with more than 8 μm spectral range were affected by the reflection of the sky, and the effect becomes larger when the angle between the IR camera and concrete surface becomes shallower, especially when the surface is smoother. They also took IR images of a bridge substructure using three types of cameras, Indium Antimonide (InSb) detector (1.5–5.1 μm), Quantum Well Infrared Photodetector (QWIP) detector (8–9 μm), and μ-bolometer detector (8–14 μm), with 45° of angle from the ground, and IR cameras equipped with QWIP and μ-bolometer detectors captured the reflected temperature of the sky. Hiasa et al. [11] reported the effect of spectral range. Long wavelength (LW: 8–14 μm [28]) cameras captured different temperatures depending on the distance, the farther objects show lower temperature readings, while a short/medium wavelength (SW/MW: 2–5.6 μm [28]) camera captured almost similar surface temperature regardless of the distance. Moreover, the areas of white lane markings captured by LW cameras showed higher temperatures than the surrounding concrete surface, while the areas taken by the SW/MW camera indicated lower temperatures than the surroundings. Nishikawa et al. [29] also mentioned that the SW/MW camera is influenced by the reflection of the sun and the contrast of the sunshine and the shade, while the LW camera is influenced by objects such as the sky and the opposite building. Thus, SW/MW cameras tend to be applied during nighttime, and LW cameras tend to be used during daytime [30]. According to Tashan et al. [5], when IR images are taken by a camera with 8–14 μm of spectral range from a farther distance, there is a possibility that temperature readings of IR images vary depending on the distance; the temperature reading at 0.7 m from the object caused a 4 °C higher reading than those at 5 and 10 m from the object. They considered that this may be due to the increase in the transmission distance between the camera and the object, and it causes more errors in the emissions readings of the IR camera. This is called atmospheric attenuation, which occurs when the atmosphere between the object and the IR camera tends to attenuate radiation due to absorption by gases and the scattering of by particles, thereby preventing the total radiation of the object from reaching the IR camera [28]. However, it is also mentioned that the atmospheric attenuation can be corrected, and if no correction is applied, the measured apparent temperature will become gradually lower with increased distance [28].

Lastly, size of delamination and the depth can be considered as the most critical factor for detectability of IRT among several factors. Some researchers indicated that it affects the detectable depth of the delamination; as the size of delamination increases, the temperature difference between sound and delaminated area also increases [23,31,32]. However, the effect of delamination size is not fully clarified yet, especially in regards to how the area, thickness and volume of delamination affect the detectability of IRT due to insufficient experimental data. Consequently, each researcher has utilized artificial defects of different sizes and concluded different detectable depths for IRT. For example, even a 3.2 cm (1.25 in.) deep delamination [14.5 cm^2 (2.25 $in.^2$)] was not detected in [33] while a 15.2 cm (6 in.) deep delamination [3,721 cm^2 (576 $in.^2$)] was detected in [24]. Another study presents that delaminations of 900 cm^2 in size were detected up to 7.6 cm deep, even though IRT could not detect it when installed at a depth of 12.7 cm [21]. One of the difficulties for NDE tests is making test specimens since those specimens become relatively huge to simulate concrete bridges. Making several sizes of delamination, embedding several depths from the surface, and handling them under different conditions are very difficult; thus, limited test specimens have been utilized for IRT experiments under limited conditions such as passive/active IRT conditions, fixed orientations and limited locations (weather conditions). Moreover, since IRT results depend on the time of data collection under the passive condition, the IRT test requires several instances of data collection, as many as possible, to assess the effect of time of data collection. The effect of data collection time might also depend on the region (weather conditions).

Under such situations, the use of FE model simulation has been increasing recently to simulate the temperature distribution of the object's surface [13,19,34–38]. In order to overcome the limitation, Hiasa et al. [18] utilized FE model simulation to explore sensitive parameters for effective utilization of IRT. After FE models were validated using the findings from the experimental counterparts, critical parameters and factors of delamination detectability regarding the size of delamination (area, thickness and volume) were explored by using the FE models. Through the FE model simulations, it was found that the most critical factor is the area of delamination; subsequently, the thickness affects the temperature differences of the surface between sound and

delaminated areas. The volume of delamination is not a significant parameter for interior damage detection using IRT since a smaller volume of delamination (270 cm^3: $30 \times 30 \times 0.3$ cm) generated larger ΔT than a larger volume of delamination (1000 cm^3: $10 \times 10 \times 10$ cm) in the FE model simulations. In addition, the FE model analysis also shows that as the area is getting larger, the impact of the thickness is also increasing [18].

3 Finite Element Model

3.1 Developed and Validated Model in the Past Study

Previously, in order to explore the favorable time window for concrete bridge deck inspections by IRT, a field experiment was conducted on December 19, 2015, at the University of Central Florida [10]. For the experiment, two test specimens with delaminations at 1.3 cm (0.5 in.) and 2.5 (1 in.) cm depths from the surface were used, and both concrete blocks had the same dimensions of 91.4 cm (3 ft.) × 91.4 cm × 20.3 cm (8 in.) as shown in Fig. 2a. These test specimens were situated outside in the natural environment, which is passive IRT condition, as shown in Fig. 2b. The specimen thickness was designed to simulate a typical bridge deck in the USA. The dimensions of the artificial delamination were 10.2 cm (4 in.) × 10.2 cm × approximately 0.3 cm (1/8 in.); they were made by foamed sheet and cardboard wrapped in plastic as shown in Fig. 2a. The thermal conductivity of air located in the concrete delamination is different than that of concrete, 0.0241 W/m °C, and creates a temperature difference on the surface of the concrete structure. Foamed sheet and cardboard were chosen to generate an artificial delamination to simulate thermal conductivity properties similar to that of air. The thermal conductivity of the foamed sheet is 0.024 W/m °C; the cardboard has a lot of air internally. According to Cotič et al. [8], no significant differences were observed between the surface temperatures above polystyrene (thermal conductivity: 0.033 W/m °C) and air-filled defects. Therefore, the artificial delamination which has similar thermal conductivity can be regarded as an actual delamination.

Furthermore, a FE model with the same condition was developed in the past study by using Heat Transfer Module of COMSOL Multiphysics software. A concrete model of the same size as the concrete blocks used in the experiment, $91.4 \times 91.4 \times 20.3$ cm, was established on a larger ground, $6 \times 6 \times 1$ m, and two pieces of Styrofoam, $10.2 \times 10.2 \times 0.3$ cm, were installed inside the concrete. The depth from the surface is the same as the experiment, 1.3 and 2.5 cm. The orientation of the concrete block was also set up similar to the experiment. In the experiment, concrete blocks were placed on wooden stands to make space through which wind blows, and those concrete blocks were set up on wooden pallets as shown in the picture. However, in the model, a concrete block was put on concrete stands, which have the same height (20 cm) as the wooden stands and the pallet for simplifying the modeling and simulation. In terms of the mesh size, the "Finer" element size was selected for the concrete block in the COMSOL software among the several predefined mesh sizes for more accurate characterization. Rumbayan and Washer [34] concluded that there is a balance between computational economy and accuracy in solution, which is true for any FE modeling applications. A "Coarser" element size was selected for the mesh sizes of the delamina-

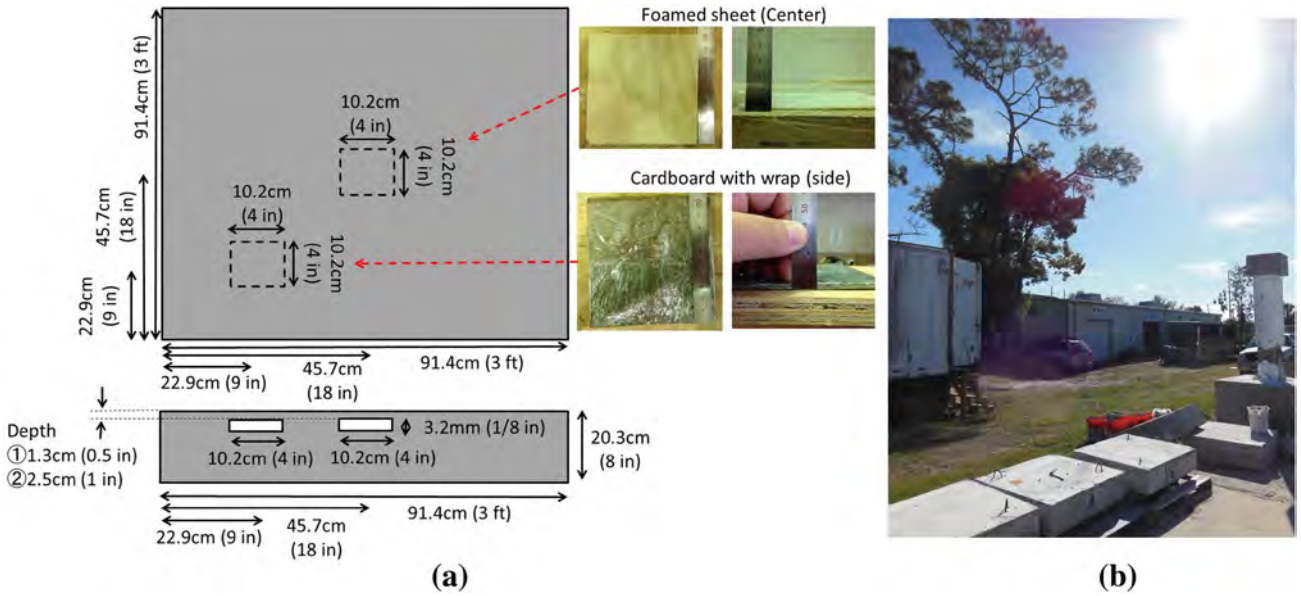

Fig. 2 Dimensions of concrete **a** test specimen and **b** test environment

Table 1 Material properties of the simulation model

Material properties	Unit	Concrete	Styrofoam	Ground
Thermal conductivity	W/(m K)	1.6	0.024	0.6
Heat capacity at constant pressure	J/(kg K)	880	1130	800
Density	kg/m^3	2300	25	1500
Solar absorptivity		0.6	–	0.94
Surface emissivity		0.88	–	0.76

tion (Styrofoam), stands of the concrete block and the ground for computational economy since it can be considered that those mesh sizes are not sensitive for concrete surface temperature. The material properties were set up as shown in Table 1.

In terms of the boundary conditions, solar radiation, air temperature and convective heat transfer were considered for each side of the concrete block in this model. The primary heat source was solar radiation in this model, the direction of sunlight (zenith angle and the solar elevation) over the simulation time was automatically computed from the longitude, latitude, time zone, date, and time by the software. The solar position is estimated by the Julian Day calendar calculation, and the zenith angle (zen) and the azimuth (azi) angles of the sun are converted into a direction vector (is_x, is_y, is_z) in Cartesian coordinates assuming that the North, the West, and the up directions correspond to the x, y, and z directions, respectively, in the model as follows [39];

$$\begin{cases} is_x = -\cos(azi)\sin(zen) \\ is_y = \sin(azi)\sin(zen) \\ is_z = -\cos(zen) \end{cases} \quad (1)$$

In this simulation, the information was set up as follows: longitude; −81.189103, latitude; 28.591897, time zone [UTC (Coordinated Universal Time)/GMT (Greenwich Mean Time)]; −5 h. The location was the test field of the previous experiment and the location information was referred to Google Maps [40]. Regarding the ambient temperature (T_{amb}), the temperature was measured throughout the day using thermocouples at the site as shown in Fig. 3. According to the record of the climatological substation, sunrise was at 7:12 a.m. and sunset was at 5:32 p.m. on that day. However, the sun started to shine on the concrete slab from 9 AM due to a tree and a building near the test site as can be seen in Fig. 2b. In this experiment, weather conditions were recorded as shown in Table 2 to check whether or not the sun was shining on the concrete surface, and whether the sky was clear or cloudy. As Vavilov et al. [38] mentioned, clouds or shadows from trees or other objects affect the results of IRT; thus, weather conditions were recorded at the same time when IRT data was collected. Table 2 also summarizes IRT results regarding whether a damage indication can be observed, and whether the time window was at a cooling or heating cycle at

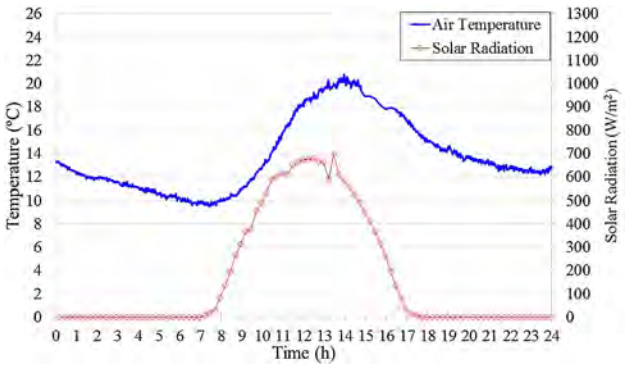

Fig. 3 Air temperature on December 19, 2015

each time. Solar irradiance (I_s) and heat transfer coefficient (h) were defined based on the record of the nearest weather station, approximately 700 m from the test site, and Fig. 3 shows the record of solar irradiance [41]. Since the maximum solar irradiance was 696 W/m^2 on that day, I_s = 700 W/m^2 was set in the software. In terms of convective heat transfer, Kumar and Mullick [42] summarized several equations of wind heat transfer coefficient provided by past research and compared it to their experimental result. In their comparative study, Sharples and Charlesworth [43] provided the closest value of wind induced convective heat transfer coefficient h_w to their experimental values as Eq. (2), and Kumar et al. [44] established highest coefficient h_w as Eq. (3);

$$h_w = 6.5 + 3.3V_w (\mathrm{W/m^2\,K}) \quad V_w \le 6\,\mathrm{m/s} \quad (2)$$

$$h_w = 10.03 + 4.687V_w (\mathrm{W/m^2\,K}) \quad V_w \le 5\,\mathrm{m/s} \quad (3)$$

The maximum wind speed was 4.9 m/s, while the maximum wind gust speed was 4.9 m/s on that day according to the climatological substation data [41]. In this software, the relational expression between temperature and heat flux boundary conditions is defined as Eq. (4);

$$q_0 = h\,(T_{ext} - T_{amb}) \quad (4)$$

where, q_0 is inward heat flux normal to the boundary (W/m^2) and T_{ext} is the temperature far away from the modeled domain [39], which is assumed as the sky temperature in the past study. Based on Eq. (2), (3) and the wind speed data,

Table 2 Summary of weather conditions and IRT results

Time	7:00 a.m.	7:30 a.m.	8:00 a.m.	8:30 a.m.	9:00 a.m.	9:30 a.m.	10:00 a.m.	11:00 a.m.	12:00 a.m.	1:00 p.m.
Sun-loading	×	×	×	×	△	◯	△	◯	◯	◯
Cloud	×	×	×	×	×	×	×	×	×	×
Indication	◯	◯	◯	◯	△	×	◯	◯	◯	◯
Cooling/heating	Cooling	Cooling	Cooling	Cooling	Cooling	N/A	Heating	Heating	Heating	Heating
Time	2:00 p.m.	3:00 p.m.	4:00 p.m.	5:00 p.m.	6:00 p.m.	7:00 p.m.	8:00 p.m.	9:00 p.m.	10:00 p.m.	11:00 p.m.	12:00 a.m.
Sun-loading	◯	△	◯	×	×	×	×	×	×	×	×
Cloud	×	×	×	×	×	×	×	×	×	×	◯
Indication	◯	×	×	◯	◯	◯	◯	◯	◯	◯	△
Cooling/Heating	Heating	N/A	N/A	Cooling	Cooling	Cooling	Cooling	Cooling	Cooling	Cooling	Cooling

Sunrise; 7:12 a.m., Sunset; 5:32 p.m.
◯: Overall irradiation (unloading); cloudy sky (Cloud); clear indication (Indication)
△: Partial irradiation (Sunloading); clear sky but some clouds (Cloud); obscure indication (Indication)
×: No irradiation (Sunloading); clear sky without cloud (Cloud); no indication (Indication)

Table 3 Specifications of IR cameras used in the past studies

Camera specifications	T420	SC5600
Detector type	Uncooled microbolometer	InSb
Thermal sensitivity (NETD)	<0.045 °C at 30 °C	<0.02 °C at 25 °C
Accuracy	±2 °C or ±2%	±1 °C or ±1%
Resolution	320 × 240 pixels	640 × 512 pixels
Spectral range	7.5–13 μm	2.5–5.1 μm
Frame rate	60 Hz	100 Hz
Field of View	25° × 19°	20° × 16°
Integration time/time constant (electronic shutter speed)	12 ms	10 μs–20 ms

$T_{ext} = T_{amb} - 50\,°\text{C}$ and $h = 30\ \text{W/m}^2\,\text{K}$ for all exposed surfaces as the heat flux boundary condition were utilized in the software through iterative trials [10].

In this experiment, an infrared camera, T420 manufactured by FLIR Systems, Inc. (Camera Specifications can be seen in Table 3), was utilized. IRT data was collected every 30 min from 7 to 10 AM and every hour thereafter until midnight, and the result was compared to FE model simulation as shown in Fig. 4. It depicts the results of the models that contain delamination at 1.3 and 2.5 cm depths, and compares temperature differences between sound and delaminated parts attained by IRT data and FE model simulation at every instance of time (21 samples in each comparison). IRT images portray the temperature difference between the sound and the delaminated part of concrete; thus, it is crucial to have temperature gradients on the concrete surface for IRT to generate thermal images indicating the existence of subsurface delamination. As can be seen in Fig. 4, there are some disparities between each ΔT obtained by IRT and simulation; however, these disparities are less than ±0.7 °C, and it can be considered within the measurement error range. Since three IR cameras with different capabilities were used at the same time, they indicated different thermal contrast between sound and delaminated parts by approximately ±1 °C at most [10]. Furthermore, it was found that different IR cameras showed different temperatures of both sound and delaminated parts approximately 0.5–3 °C depending on the camera specifications and photography angle, and indicated different ΔT even under laboratory condition [1]. Hence, even when using the same IRT method, ΔT varies depending on test conditions and camera specifications, and less than ±1 °C differences of ΔT can be regarded as "measurement error range" based on the past comparative studies. Moreover, Fig. 5 depicts the correlation of ΔT between IRT and FE model simulation results. Both 1.3 and 2.5 cm depths of delamination models show strong correlation, the R^2 are 0.91 and 0.87 respectively. Therefore, it can be concluded that this FE model was established properly, and the temperature differences between sound and damaged parts are well simulated throughout the day.

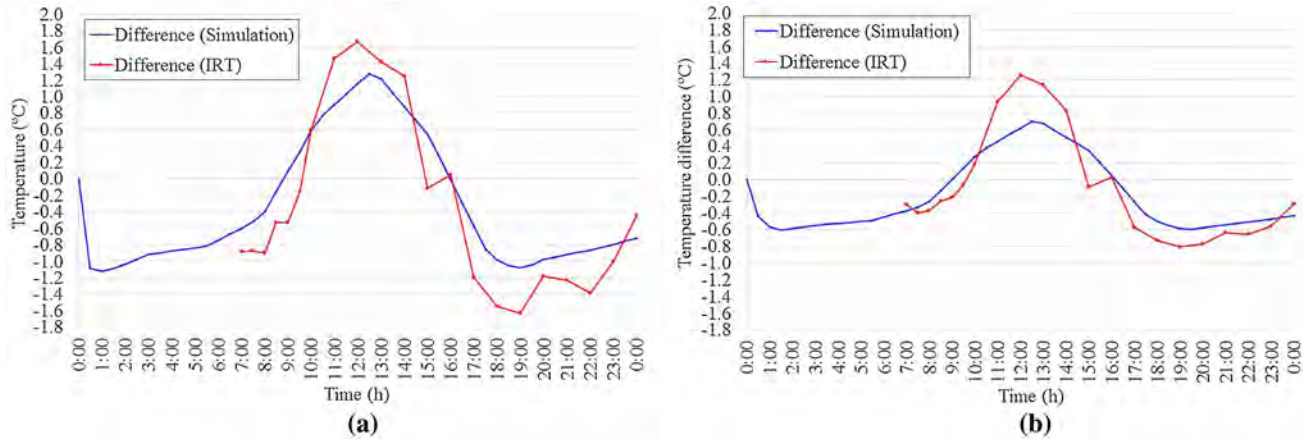

Fig. 4 Temperatures difference from IRT and simulation results. **a** 1.3 cm depth of delamination, **b** 2.5 cm depth of delamination

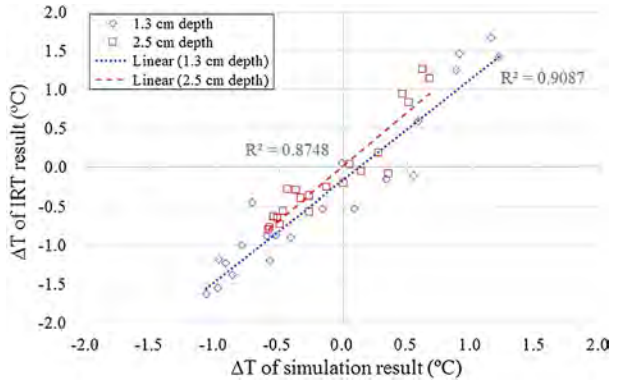

Fig. 5 Correlation of ΔT between IRT and FE model simulation results

3.2 Model Development for the Present Study

In the present study, the same weather conditions of December 19, 2015, and the same material properties for the FE model were used to reveal the effect of delamination size on the detectability of IRT. Based on this FE model, only the size of the concrete block was expanded to $300 \times 300 \times 20.3$ cm as shown in Fig. 6 and delamination shapes were changed in order to analyze the effect of a variety of delamination sizes. Some researchers indicate the impact of the length of a square's side [8], while others point out the effect of diameter/radius ratio of a delamination on its detectability by IRT [45,46]; thus, not only square shapes of delaminations, but also rectangular and circular shapes of delaminations are also modeled as shown in Fig. 7. Therefore, several types of delaminations are simulated to clarify the effects of delamination size. The delamination was modeled at the center of the concrete block in each model to avoid the effect of boundary conditions. Even though real subsurface defects cannot be ideally square, rectangle or circle shapes, ideal shapes were chosen based on a consideration of a balance between reasonableness of modeling the delaminations and the accuracy in solution. Since the objective of this study is to understand the effect of shapes and sizes of delamination on its detectability by IRT, it was considered that ideal shapes can reveal the effect of delamination size more clearly than modeling complicated real shapes of delaminations.

Regarding the depth of delamination from the surface to the top of the delamination, a depth of mainly 5.1 cm (2 in.) was applied since the top concrete cover for a bridge deck is typically 5.1 cm, and defects often occur around the reinforcing bars; thus, that depth was chosen for this analysis to explore the impact of delamination size on IRT. Since this FE modeling aims to simulate ΔT caused by the delamination, reinforcing bars were not modeled in this study. The thermal conductivity of reinforcement is much higher than the surrounding concrete, so that it can be assumed reinforcement would not cause temperature differences on the concrete surface [12]. Actually, when the artificial delaminations were installed in the concrete test specimens, guide steels were set up in the concrete in order to correctly locate the artificial delaminations at each depth, yet, those guide steels did not cause any temperature differences on the surface [10]. Therefore, it can be considered that reinforcement inside concrete is not important for passive IRT test and FE modeling, and it can be ignored. Furthermore, in order to investigate the effect of delamination depth, delaminations of 7.6 cm (3 in.) and 10.2 cm (4 in.) depths were also modeled for comparative purposes. Each delamination was installed at the middle of the concrete block as depicted in Fig. 7, and the following are the dimensions of each component of the model:

(1) *Concrete block* $300 \times 300 \times 20.3$ cm
(2) *Ground* $600 \times 600 \times 100$ cm
(3) *Stands* 10×20 cm (to make space through which wind blows)
(4) *Delamination* plane size; Table 4, thickness of delamination; 0.1, 0.3, 1, 2, 10, 15 cm

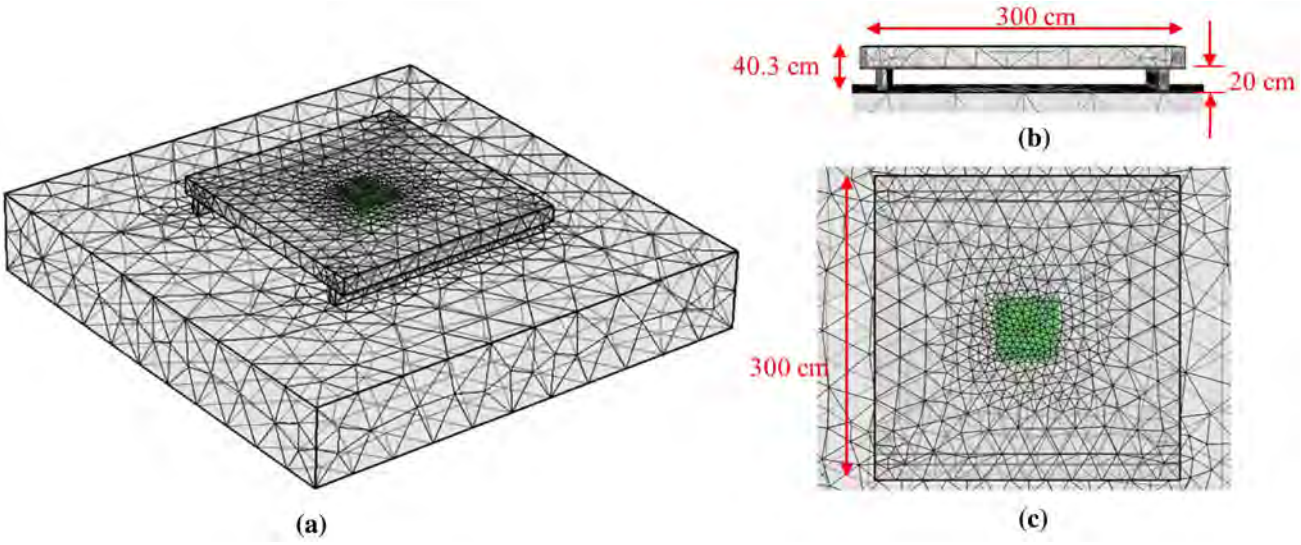

Fig. 6 Expanded FE model for this study. **a** General view, **b** cross section view, **c** plan view

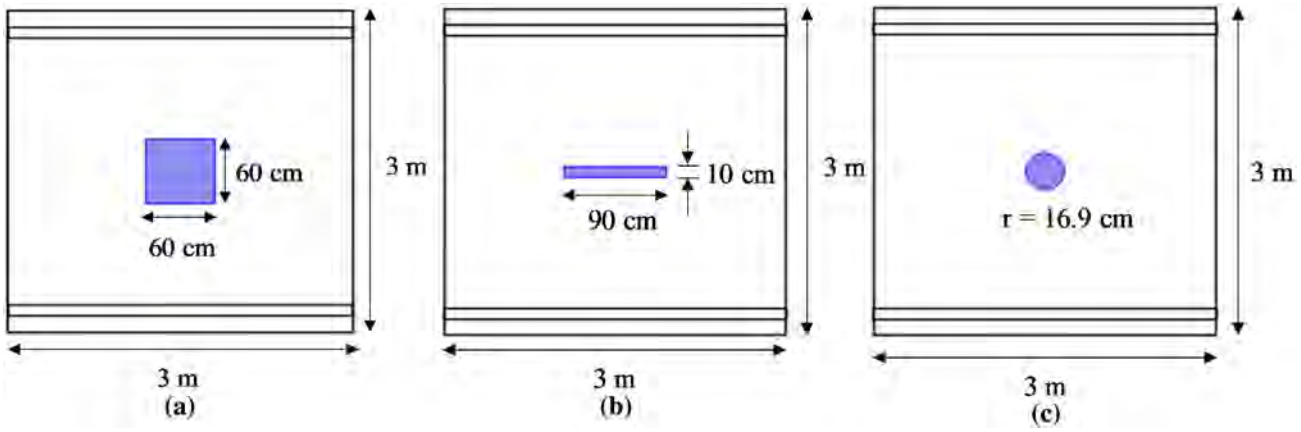

Fig. 7 Shapes of delaminations modeled (plan view). **a** *Square* (60 × 60 cm), **b** *rectangle* (10 × 90 cm), **c** *circle* (r = 16.9*cm*)

(5) *Depth of delamination* 5.1, 7.6 and 10.2 cm.

4 Simulation Results

4.1 Reference Points of the Temperatures at Sound and Delaminated Areas

All simulations aim to compare temperature differences between sound and delaminated areas (ΔT) since ΔT is the most important factor for IRT to identify the existence of subsurface delaminations from thermal images. Even though concrete deck surfaces of different colors caused by stains, patched parts, lane markings and other obstacles such as gravel, debris and trash create different temperatures compared to the surroundings in the same way as a delamination does, those can be easily distinguished by comparing the visual images and IRT images [10,11]. Thus, this study treats ΔT as the factor of IRT detectability for subsurface defect detection. According to Clark et al. [47], the effective delamination detection range of ΔT was found to be approximately 0.2–0.3 °C. Hiasa et al. [18] also assumed that within ±0.3–0.4 °C of ΔT was the undetectable band of ΔT for IRT. Although, more experimental data under different experimental and environmental conditions may be needed, a probable range for undetectability can be assumed to be within approximately ±0.2 °C of ΔT, a probable range for detectability is between ±0.2 to 0.4 °C, and an almost certain range for detectability using IRT is anything above ±0.4 °C as shown in Fig. 8. However, the concrete surface is not a homogeneous temperature even under laboratory test conditions, and each pixel of an IR image has a different temperature [1]. Therefore, in order to obtain each model's ΔT properly from the simulation results for comparison purposes, the same points of delaminated and sound areas should be decided beforehand. In this study, each tem-

Table 4 Plan size of modeled delaminations

Square Depth: 5.1, 7.6 and 10.2 cm		Rectangle Depth: 5.1 cm				Circle Depth: 5.1 cm	
Size (cm)	Area (cm^2)	Size (cm)	Area (cm^2)	Size (cm)	Area (cm^2)	Radius × Thick (cm)	Area (cm^2)
$10 \times 10 \times 0.3$*	100	$5 \times 80 \times 0.3$	400	$10 \times 90 \times 0.3$	900	11.3×0.3	400
$15 \times 15 \times 0.3$	225	$8 \times 50 \times 0.3$	400	$15 \times 60 \times 0.3$	900	16.9×0.3	900
$20 \times 20 \times 0.3$*	400	$10 \times 40 \times 0.3$	400	$20 \times 45 \times 0.3$	900		
$30 \times 30 \times 0.3$*	900	$16 \times 25 \times 0.3$	400	$25 \times 36 \times 0.3$	900		
$40 \times 40 \times 0.3$*	1600						
$50 \times 50 \times 0.3$	2500						
$60 \times 60 \times 0.3$	3600						

* Different thicknesses were modeled at 5.1 cm depth: 0.1, 1, 2, 10, 15 cm

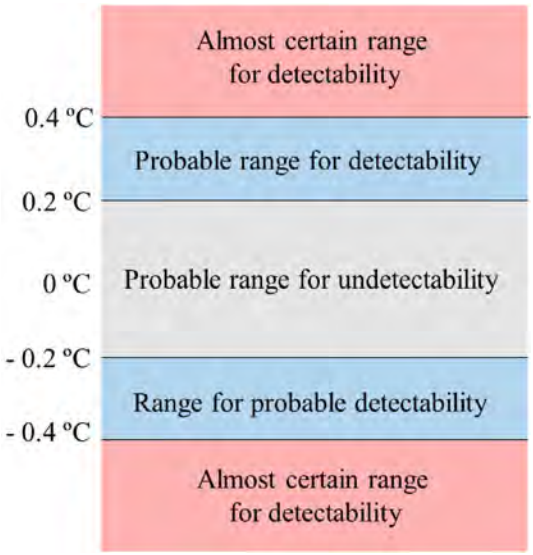

Fig. 8 Assumed potential detectable and undetectable ΔT range

perature of sound (T_s) and delaminated (T_d) part and ΔT are defined as follows:

T_s: almost homogeneous temperature at sound area

T_d: maximum or minimum temperature at delaminated area

$$\Delta T = T_d - T_s \tag{5}$$

It can be assumed that a slightly larger/smaller area than the real delamination size shows the temperature difference on the concrete surface, and other sound areas have almost the same temperature as shown in Fig. 9. Therefore, several points of temperatures were compared as shown in Fig. 10 to verify the assumption. Regarding the delaminated area, temperatures of the center part and 10 cm away from the center as shown in Fig. 10a were compared ("$T_{del}(0)$-$T_{del}(10)$" in Fig. 10b). As to the sound area, the temperature differences between the center part and points of 1, 5 and 10 cm away from the edge of the delamination as depicted in Fig. 10a were compared, and each temperature difference is shown as "ΔT(1)", "ΔT(5)" and "ΔT(10)" respectively in Fig. 10b. In the figure, the result of a delamination with the size of 30 × 30 cm is displayed. As it was assumed in Fig. 9, the center part of the delamination showed higher/lower temperature than the surrounding delaminated area during the daytime/nighttime as shown in Fig. 10b, "$T_{del}(0) - T_{del}(10)$"; thus, the center part of the delamination was chosen as the reference point of the delaminated part.

In terms of the sound part, sound areas clearly indicate different temperatures compared to delaminated areas, yet, the point of 1 cm away from the edge shows slightly different ΔT, 0.14 °C at most, compared to the other two points throughout the day. On the other hand, these two points, 5 and 10 cm away from the edge, show almost the same ΔT, 0–0.03 °C differences from each other at any time in a day. The same results can also be obtained from other delamination size models. Therefore, these results indicate that a slightly wider area, about 1 cm from the edge in this case, than the real delamination size shows the temperature difference on the concrete surface, and other sound areas have almost the same temperature as shown in Fig. 9. Thus, the point of 10 cm away from the edge of delamination was selected as the reference point for a temperature of the sound part.

4.2 Effect of Delamination Thickness

The effect of delamination thickness was investigated since Hiasa et al. [18] found that as the delamination area is getting larger, the impact of the delamination thickness is also increasing. However, it is not enough to clarify the effect of the delamination thickness since only two different thicknesses, 0.3 and 1.0 cm, of delaminations were compared in the previous study. It is also important to determine whether or not ΔT is getting bigger as the thickness of delamination is getting thicker, or if it converges to a certain value at a

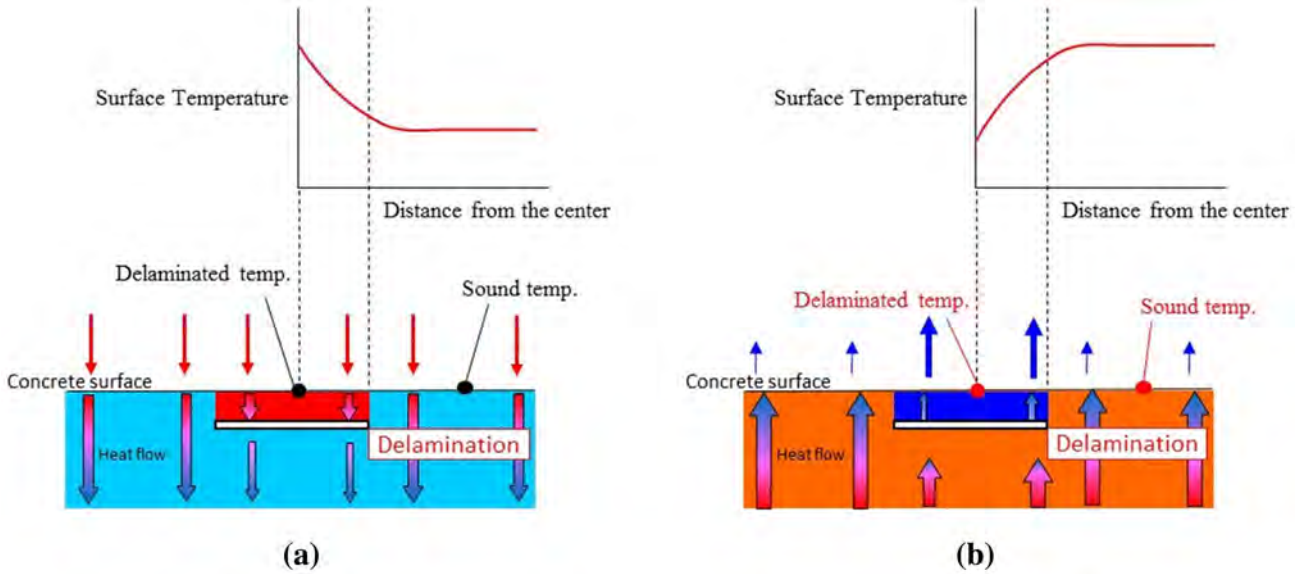

Fig. 9 Images of delaminated concrete surface temperature. **a** Daytime period, **b** nighttime period

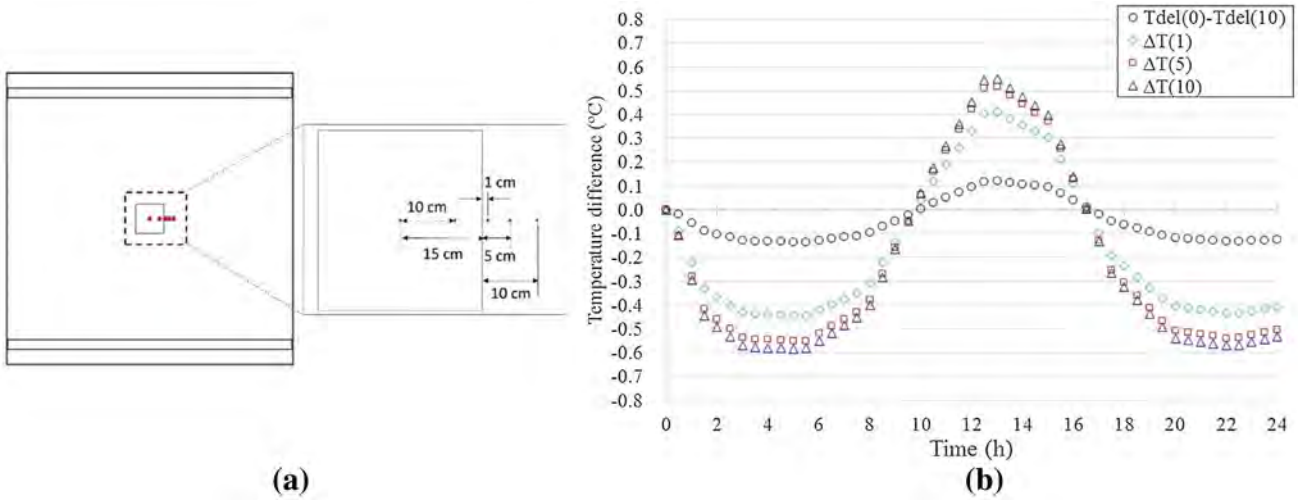

Fig. 10 Compared points at sound and delaminated areas. **a** Location of each point, **b** temperature differences between center part

certain thickness of delamination. Therefore, a larger variety of sizes of delaminations were modeled in this study. Thus, several thicknesses of delaminations, 0.1, 0.3, 1, 2, 10 and 15 cm, were modeled and analyzed. Regarding the shape and size of delamination, a square shape with four different areas of delaminations were used, 10×10, 20×20, 30×30, and 40×40 cm, and those delaminations were located at a depth of 5.1 cm from the surface. Figure 11 compares ΔT of each delamination thickness in respective areas of delamination. As it was assumed in Fig. 1, the delaminated area showed higher temperature (lower temperature) than the sound area during the daytime (nighttime) at any sizes of delamination. Furthermore, it is obvious that the difference of ΔT between 0.1 and 15 cm thicknesses is getting bigger as the area is getting larger; the maximum difference between two thicknesses is 0.16 °C in 10×10 cm delamination model while it is 0.75 °C in 40×40 cm delamination model. In terms of 20×20 and 30×30 cm delamination models, they generated 0.45 and 0.65 °C differences at most, respectively. As can be seen from each graph, it is also obvious that 0.1 cm of thickness generates the smallest ΔT despite the area of delamination; consequently, 0.3 cm of thickness yields a smaller ΔT than the other thicker delaminations. However, 1, 2, 10 and 15 cm thicknesses of delaminations generate almost the same ΔT, less than 0.15 °C difference at most among these four thicknesses at any time and any areas of delaminations. Fig. 12 depicts differences of ΔT between (a) 0.3 and 0.1 cm thicknesses, (b) 1 and 0.3 cm thicknesses, (c) 2 and 1 cm thicknesses, (d) 10 and 2 cm thicknesses, and (e) 15 and 10 cm thicknesses for each area

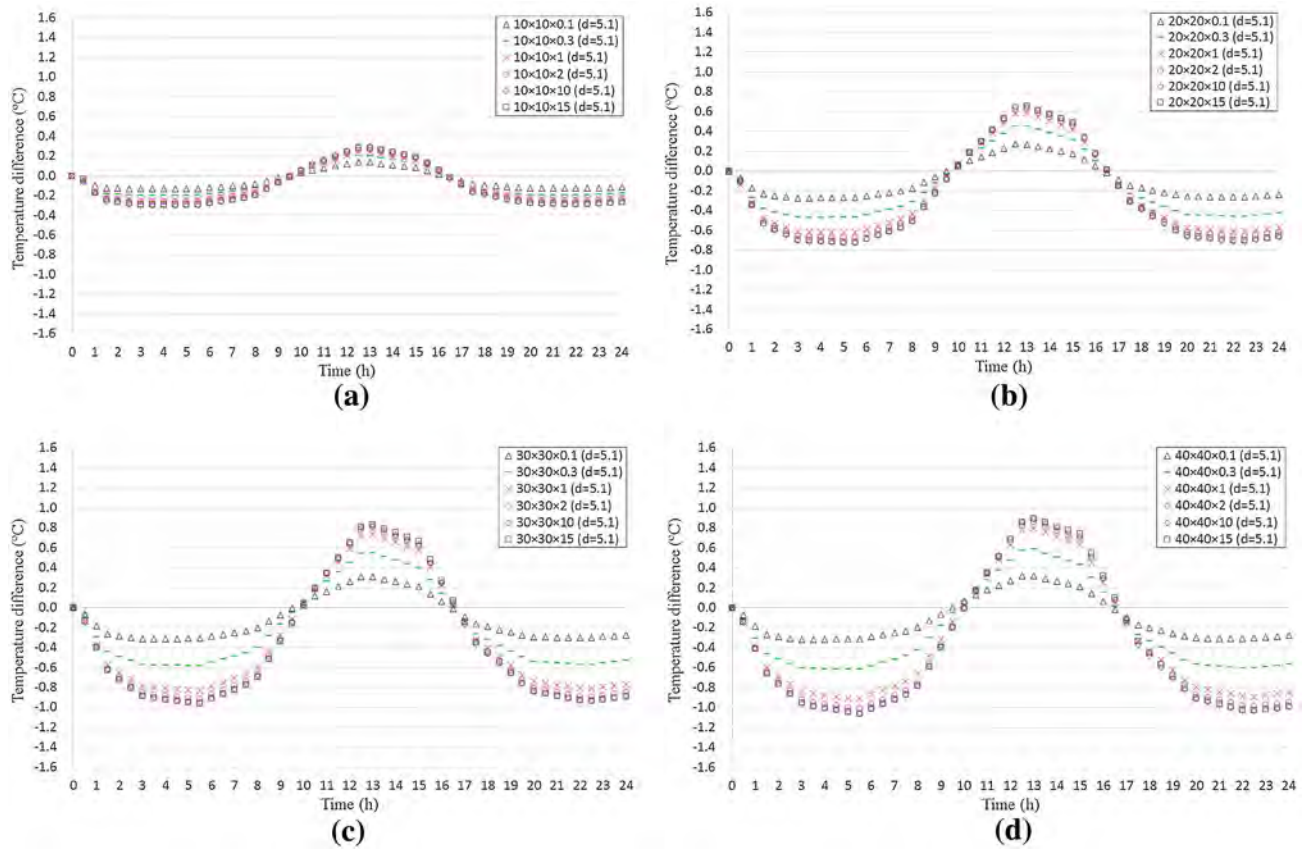

Fig. 11 Temperature differences with respect to delamination sizes. **a** 10 × 10 cm (5.1 cm depth), **b** 20 × 20 cm (5.1 cm depth), **c** 30 × 30 cm (5.1 cm depth), **d** 40 × 40 cm (5.1 cm depth)

of delamination. As mentioned above, Fig. 12a, b show larger differences as the area becomes larger. Moreover, Fig. 12c–e do not indicate a significant difference regardless of thickness and area of delamination. Therefore, these results show that delamination thickness affects ΔT and a thicker delamination generates larger ΔT. Furthermore, the effect of thickness increases as the area increases; however, the effect of delamination thickness converges to a certain point of ΔT when the thickness of delamination becomes 1 cm or more.

4.3 Effect of Delamination Area and Shape

In this subsection, the effects of delamination area and shape were investigated. In the previous study conducted by Hiasa et al. [18], only square shape delaminations comprising of three different areas, 10 × 10, 20 × 20 and 30 × 30 cm, were compared by the FE model simulations. Hence, the effects of delamination area and shape were not fully investigated. Several square shapes of delaminations were compared in the present study to clarify whether the effect of delamination area converges to a certain value or not. In the model of delaminations, lengths of a side of a square (L) were changed such as L = 10, 15, 20, 30, 40, 50 and 60 cm as summarized in Table 4. Every thickness of the delamination was set to 0.3 cm in these cases for keeping consistency with the test specimen used for the field experiment. Figure 13a depicts the simulation result of each delamination model located at 5.1 cm depth. It is obvious that the area of delamination strongly affects ΔT. However, as the delamination area exceeds 30 × 30 cm, the corresponding increase in ΔT is reduced, at most 0.05 °C between 30 × 30 and 60 × 60 cm. In fact, when the areas become greater than 40 × 40 cm, the differences of ΔT for each delamination area are less than 0.01 °C at any time. Therefore, it can be concluded that ΔT converges to a certain value when the delamination area is approximately 40 × 40 cm. Furthermore, in order to investigate whether or not the depth of delaminations from the surface also affects ΔT in addition to the area of delamination, the same areas of delaminations at 7.6 and 10.2 cm depths were modeled and simulated. The result is displayed in Fig. 13b, c. It is obvious that the delamination at 7.6 cm depth generated smaller ΔT than the delamination at 5.1 cm depth at any time; ΔT was decreased at most 0.38 °C for L = 50 and 60 cm models as the location of the delamination becomes deeper from 5.1 to 7.6 cm. Moreover, when the depth of delamination becomes deeper, 10.2 cm, ΔT

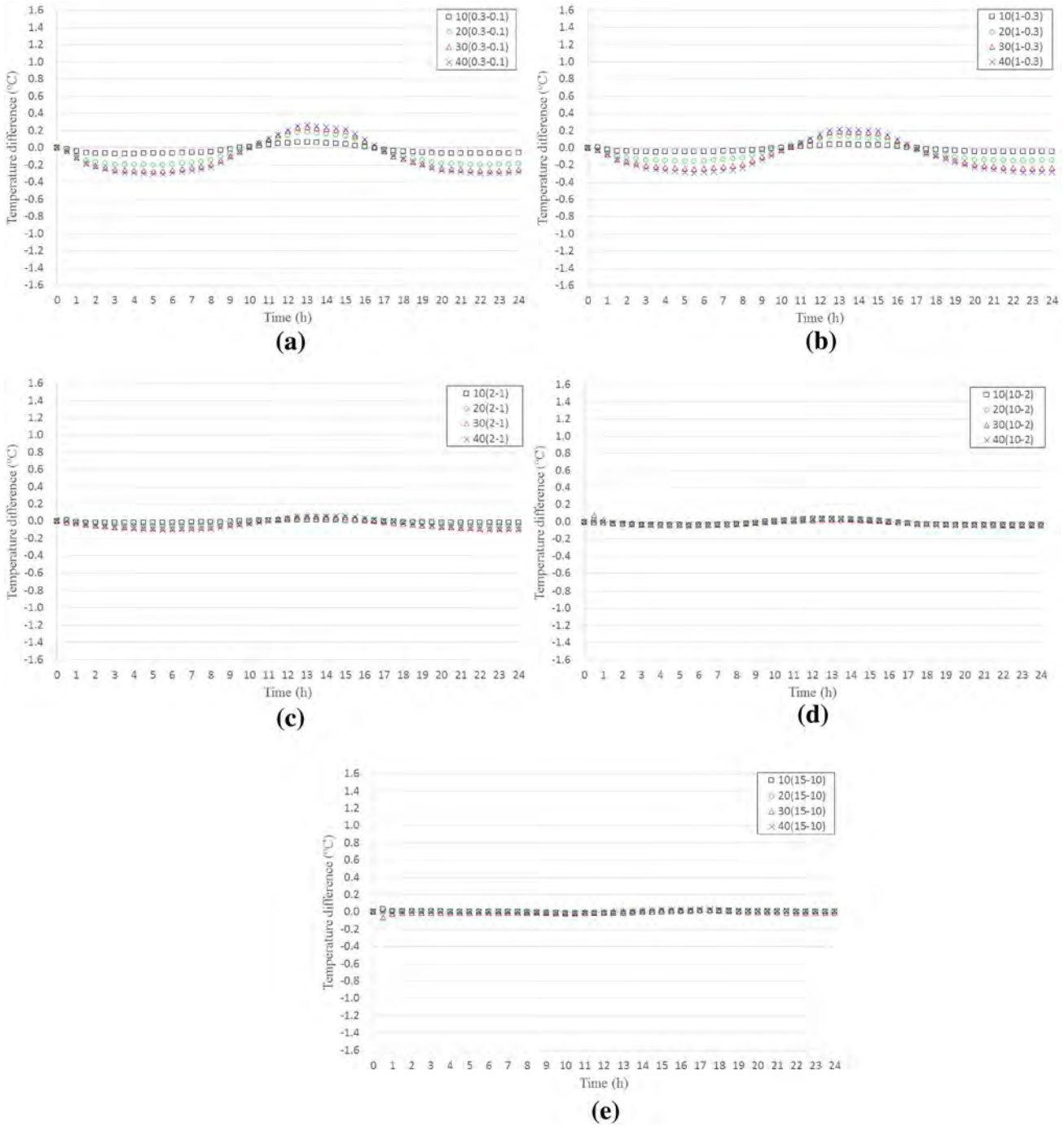

Fig. 12 Effect of delamination thickness on ΔT depending on the area. **a** Comparison between 0.3 and 0.1 cm thickness, **b** comparison between 1 and 0.3 cm thickness, **c** comparison between 2 and 1 cm thickness, **d** comparison between 10 and 2 cm thickness, **e** comparison between 15 and 10 cm thickness

decreased at most 0.22 °C for L = 60 cm model compared to the model at 7.6 cm. Furthermore, as can be seen in Fig. 13, the depth of delamination affects ΔT more during the daytime than during the nighttime under the given conditions. Even though more experimental data is needed, this result supports the conclusion that the preferable time period to apply IRT for concrete bridge deck inspection is during the nighttime cooling effect [10]. The maximum difference of ΔT between 30 × 30 and 60 × 60 cm was 0.07 °C in both cases of 7.6 and 10.2 cm depths delaminations. These results support the conclusion that the size of delamination also affects detectability of IRT in addition to the data collection time and the depth of delamination from the concrete surface. As for the convergence issue regarding the area of

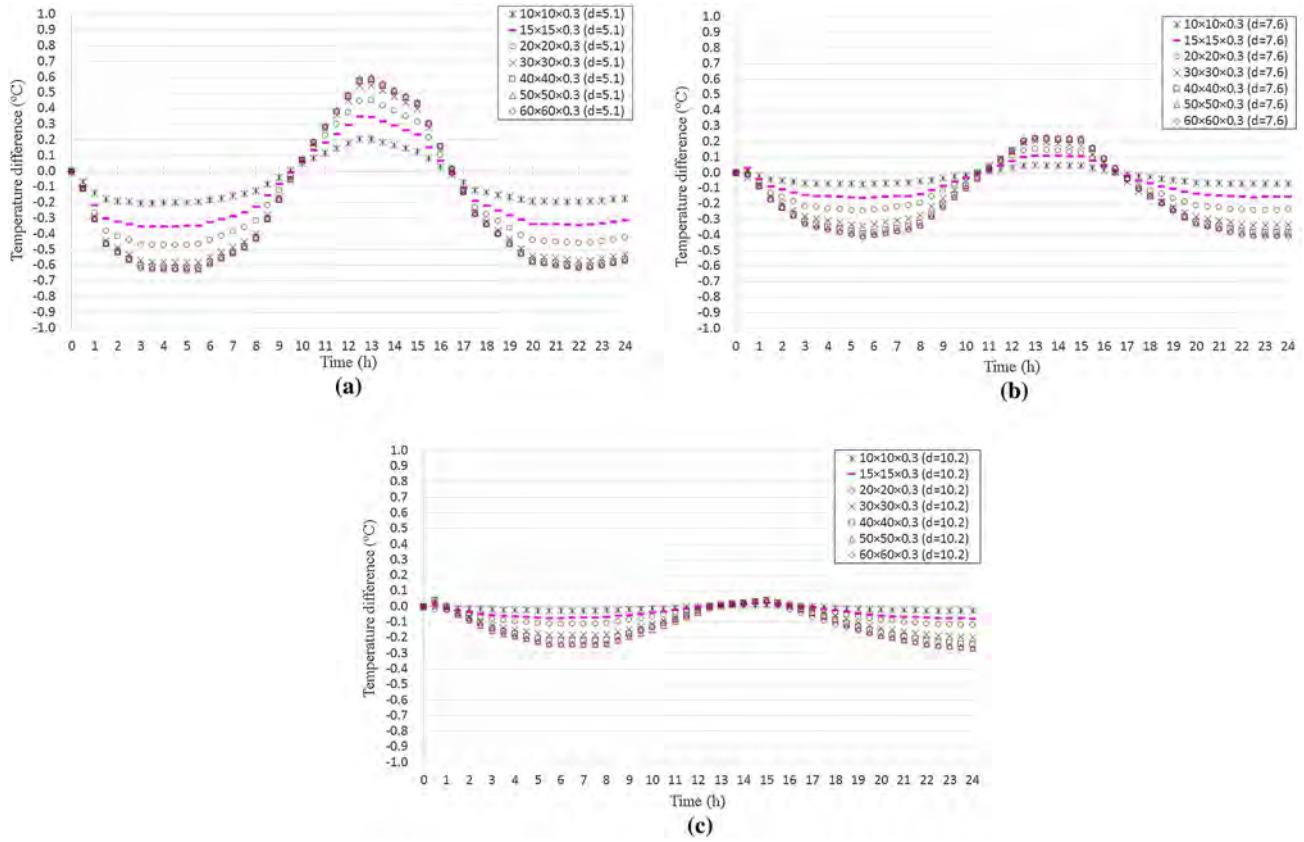

Fig. 13 Comparison of ΔT with different square shape areas of delaminations. **a** L × L × 0.3 cm (5.1 cm depth), **b** L × L × 0.3 cm (7.6 cm depth), **c** L × L × 0.3 cm (10.2 cm depth)

delamination, ΔT of the models of 7.6 and 10.2 cm depths delaminations also converged to a certain point when the delamination area is approximately ΔT of 40 × 40 cm; thus, it can be concluded that ΔT converges to a certain value when the shape of delamination is square and its area is approximately 40 × 40 cm regardless of its depth.

In terms of detectability of delaminations by IRT, when a delamination exists at 5.1 cm depth and its size is 15 × 15 × 0.3 cm or larger, IRT may be able to detect this delamination since these types of delaminations generated more than 0.3 °C of ΔT, which exceeds the range for probable detectability which is approximately ±0.2–0.4 °C range. Regarding the 7.6 cm depth of delamination, 20 × 20 × 0.3 cm or larger delaminations might be detected mainly during the nighttime cooling cycle if IRT is used for such delaminations since those delamination models show ±0.2–0.4 °C range of ΔT in a day. In terms of the 10.2 cm depth of delamination, 40 × 40 × 0.3 cm or larger delaminations might be detected only during the nighttime cooling cycle. Fig. 14 shows some visual images of simulation results of (a) 15 × 15 × 0.3 cm, (b) 30 × 30 × 0.3 cm, and (c) 60 × 60 × 0.3 cm. As it is assumed, all delaminated parts can be clearly seen for the 5.1 cm depth delamination models at 1 p.m. (daytime) and 10 p.m. (nighttime). As to the 7.6 cm depth delamination models, indications during the daytime are less clear than those during the nighttime, and it is difficult to distinguish the indication of a 15 × 15 × 0.3 cm delamination during the daytime. Even though the indication of a 15 × 15 × 0.3 cm delamination at 10 p.m. can be distinguished from the simulation result, it can be assumed that detecting this size of delamination at 7.6 cm might be difficult under passive IRT since the concrete surface must have a different temperature gradient on the surface, and it might be considered as noise. Regarding the 10.2 cm depth delamination models, no indication can be observed during the daytime while the 60 × 60 × 0.3 cm delamination model shows an indication during the nighttime. As for the 30 × 30 × 0.3 cm delamination model, it shows a slight indication on the simulation result, yet it is uncertain that the delamination can be detected by IRT under passive condition since the ΔT, −0.18 °C, is close to the border between the assumed ranges for detectability and undetectability, −0.2 °C. From these results, it can be concluded that as the area of delamination becomes larger, the effect on its detectability by IRT becomes bigger; however, if the area becomes more than 30 × 30 cm, the effect of delamination area starts to diminish. The temperature difference ΔT converges to a certain value when the delamination area is approximately 40 × 40 cm.

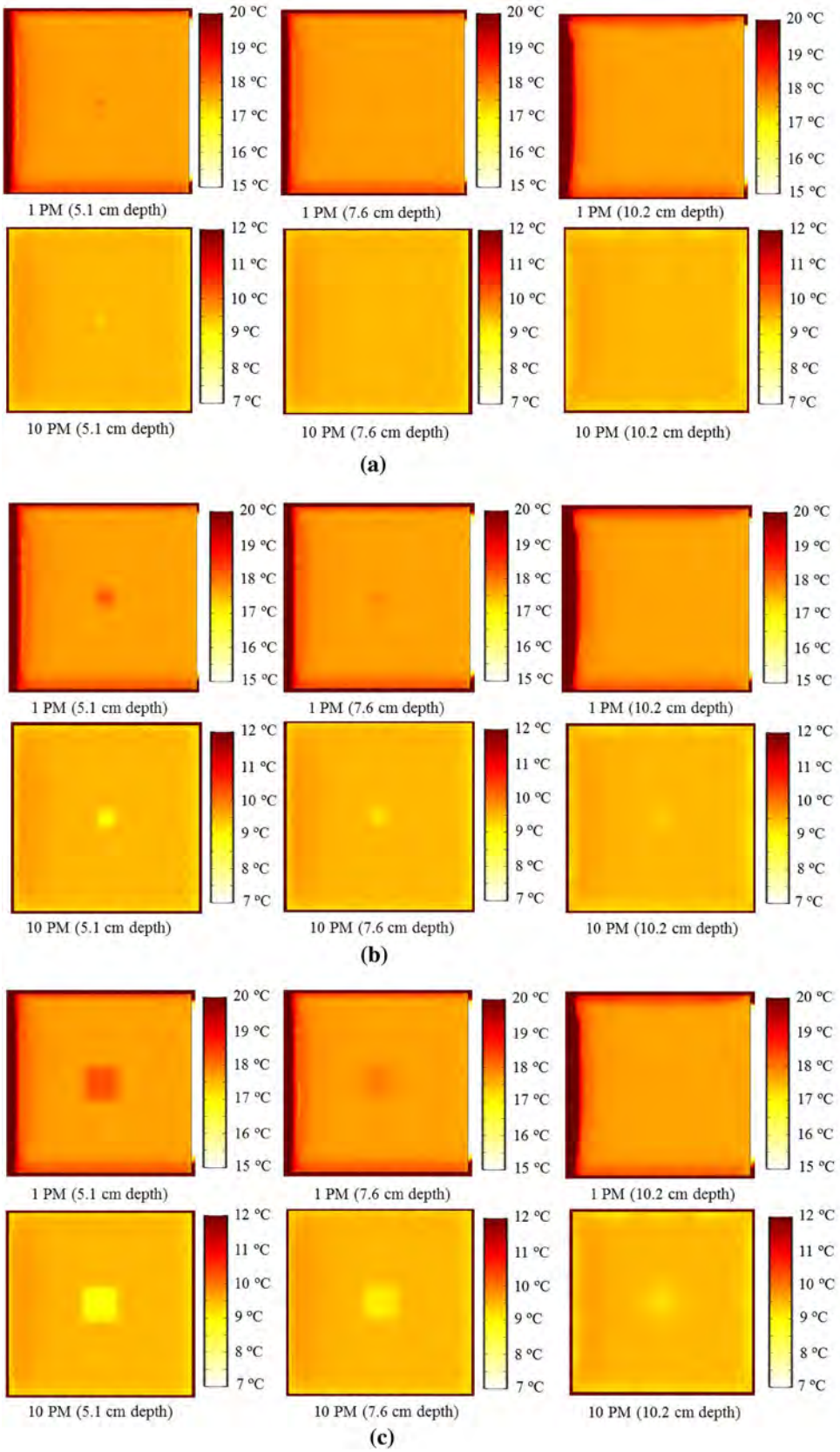

Fig. 14 Simulation results at each depth (L = 15, 30 and 60 cm; 1 p.m. and 10 p.m.). **a** 15 × 15 × 0.3 cm, **b** 30 × 30 × 0.3 cm, **c** 60 × 60 × 0.3 cm

Table 5 Size of delaminations of each area

Area (cm^2)	400				900			
Length of sides (cm)	5×80	8×50	10×40	16×25	10×90	15×60	20×45	25×36
Ratio of length (%)	6	16	25	64	11	25	44	69

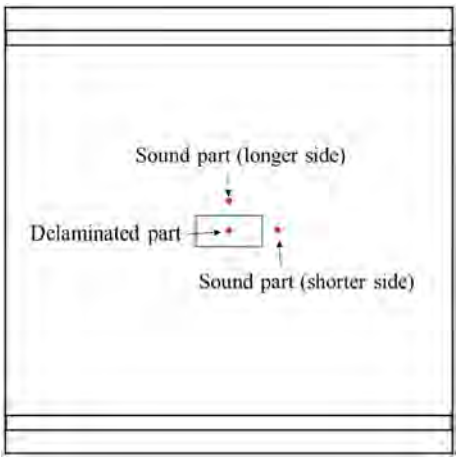

Fig. 15 Reference points of delaminated and sound parts for *rectangle* shaped delamination

Since the effects of area and thickness for square-shaped delaminations were clarified above, the effects of several other shapes of delaminations such as rectangles and circles were also modeled and analyzed. Rectangles and circles with two fixed areas of delaminations, 400 and 900 cm^2, were modeled in the simulations and compared to ΔT of the same area of square. In terms of the sizes of rectangles, four different shapes of rectangles were modeled and the ratios of lengths of shorter side to longer side were summarized in Table 5. Regarding ΔT of rectangles, two sides of the sound part's temperature were compared as shown in Fig. 15 in order to investigate how rectangular-shaped delaminations affect the temperature gradients of the concrete surface. Fig. 16 depicts the results of the two cases. "L" in the legends of these graphs means the temperature at 10 cm away from the edge of the longer side of the rectangle, and "S" indicates the temperature at 10 cm away from the edge of the shorter side of the rectangle. Regarding the differences of ΔT between longer and shorter sides of delaminations, the maximum difference between two sides was 0.01 °C in each model throughout the day. Therefore, there is no significant difference in regard to ΔT between the longer side and the shorter side for rectangle delaminations.

However, comparing both cases of Fig. 16, some rectangle delaminations showed smaller ΔT than others even though they have the same area as the others while square, circle and some rectangular-shaped delaminations of the same area generated similar ΔT; in the case of 400 cm^2 of delaminations, the maximum difference of ΔT was 0.03 °C among the square and circle models and 16×25 cm of the rectangle model. In terms of 900 cm^2 of delaminations, it was 0.05 °C at most between the circle and 20×45 cm of the rectangle models. Moreover, the result showed that only rectangles which have 25% or lower ratios of the shorter side length to the longer side length generated distinctly smaller ΔT than the other delaminations which have the same area in each case; 5×80, 8×50, 10×40 cm for 400 cm^2, 10×90, 15×60 cm for 900 cm^2. It can be assumed that if the aspect ratio (ratio of the length of the shorter side to the longer side of the delamination) is more than 25%, ΔT of any delaminations converges to ΔT of the same area of a square/circular-shaped delamination. Furthermore, from these two cases of Fig. 16, it can be concluded that if the aspect ratio is 25% or smaller, ΔT becomes smaller than the ΔT of the same area of a square/circular-shaped

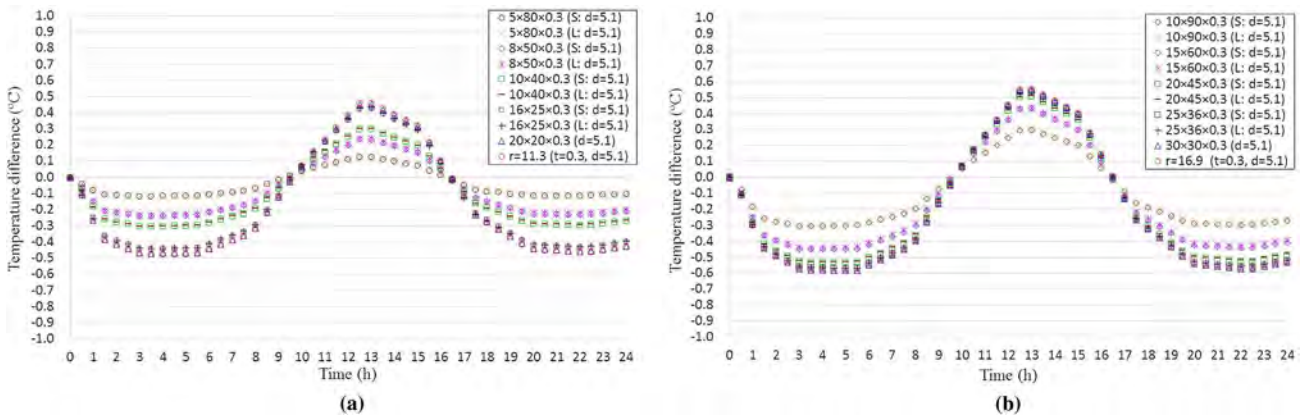

Fig. 16 Temperature differences depending on the shape of delamination. **a** 400 cm^2 (0.3 cm thickness; 5.1 cm depth), **b** 900 cm^2 (0.3 cm thickness; 5.1 cm depth)

delamination, and it is getting smaller as the ratio becomes smaller.

5 Estimation of Delamination depth from IRT Data

Although IRT can indicate the location of the delamination, one of the biggest limitations is that it cannot provide data about the depth of the delamination [2,22]. However, there is a strong correlation between the size of delamination and the depth from the surface in regard to the temperature difference of the concrete surface between delaminated and sound parts as discussed in Sect. 4. Generally, IRT provides only a potential delaminated area by capturing temperature differences between sound and delaminated parts. However, based on the given delaminated area and the temperature difference, it can be assumed that inverse analysis can be conducted using FE modeling by simulating several depths and thicknesses of delamination models with the indicated area. Therefore, the findings of the current study show that there is a possibility to estimate the depth of the delamination even when using IRT, leading IRT to a great improvement for concrete structure inspections.

In order to investigate the possibility whether or not IRT can provide information about the depth of delamination, IRT data from real bridge deck scanning was utilized in this section. As shown in Fig. 17a, a hatched area of the bridge deck was inspected by several NDE methods by other researchers [22,48]. The test bridge is Haymarket Bridge, which is part of VA Route 15 running over Interstate 66 in Haymarket, Virginia. In the field test, 8 core samples were drilled after the data collection of each NDE method, and Fig. 17b shows one of the 8 cores drilled at the circle located at the coordinate of F-16 described in Fig. 17c. The grid line was assigned at intervals of 60 cm [22,48]. Hiasa et al. [11] scanned the same location with IRT at a normal driving speed without lane closure during nighttime on October 2, 2014, and compared the result to other NDE methods such as IE, GPR and chain drag. Figure 18a shows the visual image of the bridge deck taken by a line camera system, and Fig. 18b is the result of IRT, which is processed by an infrared image processing software with a specialized algorithm [49], taken by a cooled type camera, SC5600 manufactured by FLIR Systems, Inc. (Camera Specifications can be seen in Table 3). The indications enclosed by dotted lines in Fig. 18b are the potential delaminations detected by IRT. Even though there is no evidence which indications are correct or incorrect except for the locations of 8 core samples, IE and chain drag indicated almost identical shapes as shown in Figs. 17b and 18b; thus, Hiasa et al. [11] concluded that high-speed scanning with a cooled type camera can provide a similar level of damage detection to IE and chain drag, which are considered as accurate methods among several NDE methods used in the past research by other researchers [22,48].

In the present study, the depth of delamination located in the grids from 15–17 and E–G in Fig. 18b was estimated. The depth of the delamination can be assumed to be about 6 cm from the image of the core since the top concrete cover is 6 cm and the delamination occurred around the reinforcing bar due to corrosion [48]. Although the delaminated cores must have been repaired by grouting after core sampling in the past research, it can be considered that the surrounding parts are still delaminated at the same depth of the core sample as shown in Fig. 17b because there is no mark of repair work such as patching around the mark of grouting at the coordinate of F-16 as shown in Fig. 18a; thus, the delamination can be assumed as one delamination as enclosed by the dotted line. Therefore, that particular delamination enclosed by a dotted line, which are indicated by the coordinates from 15–17 and E–G in Fig. 18b, was chosen to investigate the depth in this study. Regarding the size of delamination, the area of the delamination can be considered more than 40×40 cm since one grid line is 60 cm in Fig. 18b and that delam-

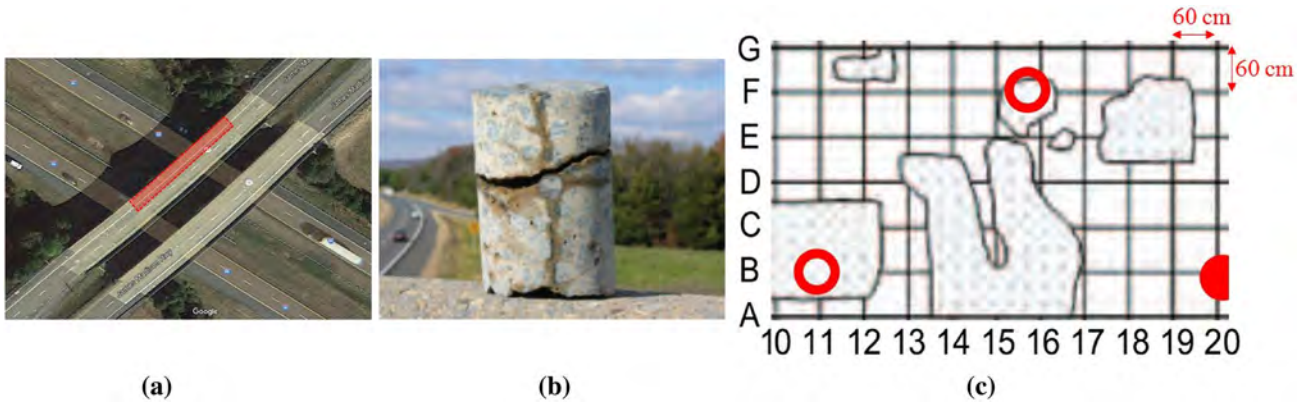

Fig. 17 Applied bridge (**a**), the core (**b**) and indicated delaminations (**c**) (*source* [22,40]). **a** Tested bridge, **b** core sample (F-16), **c** indicated delaminations by chain drag

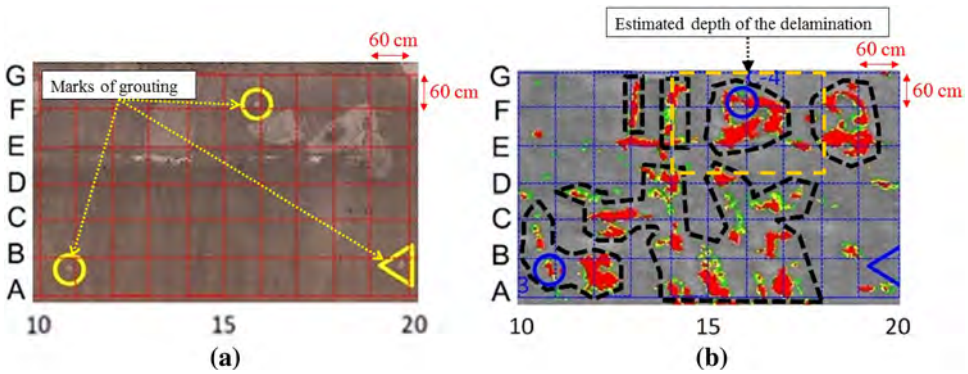

Fig. 18 Visual and processed IR images of the same area as Fig. 11c, d (*source* [11]). **a** Visual image, **b** processed IR image

ination occupies approximately one and a half grids in both horizontal and longitudinal coordinates.

Since ΔT converges to a certain value for these types of delaminations as discussed in Sect. 4, a 40×40 cm square-shaped delamination model is used in this analysis to estimate the depth from the surface. The delamination thickness is also an unknown parameter in addition to the depth of delamination. Two sizes of thicknesses, 0.1 and 1 cm, were modeled in the present study. As mention in Sect. 4.2, the effect of thickness converges to a certain point of ΔT when the thickness of delamination reaches at least 1 cm. ΔT of these two sizes of delaminations were assumed to be minimum ΔT, which is ΔT of $40 \times 40 \times 0.1$ cm, and maximum ΔT, which is ΔT of $40 \times 40 \times 1$ cm. The authors assumed it is possible to estimate the depth of delamination by comparing ΔT from IRT data with the minimum and maximum ΔT obtained from FE model simulations at several depths.

As for ΔT of IRT data, temperatures of delaminated and sound parts were defined by picking three points randomly from the respective parts of IRT data and calculating the averages of the selected points. Fig. 19 is the enlarged infrared image of the delamination located at coordinates between 15–17 and E–G in Fig. 18. The three temperatures written in red color are the temperatures of the delaminated part and other three written in green color are the temperatures of the sound part. From Fig. 19, the temperature of the sound part was found to be 19.02 °C, and the temperature of the delaminated part was 18.69 °C. Hence, ΔT was −0.33 °C.

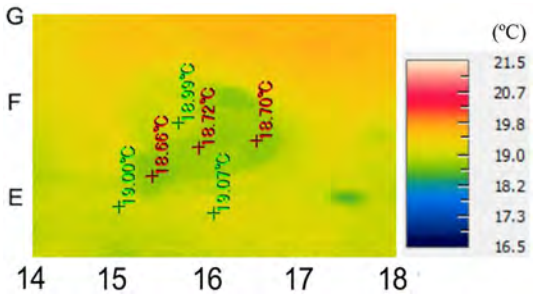

Fig. 19 Temperatures of delaminated and sound parts

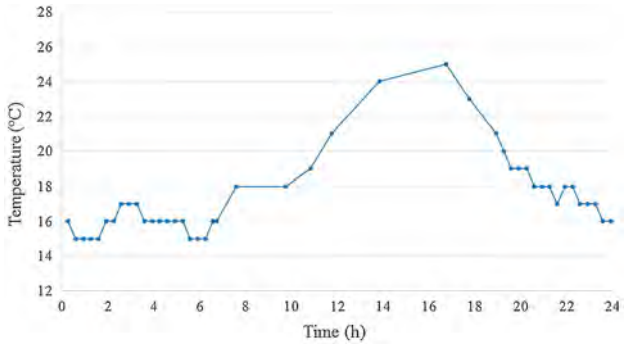

Fig. 20 The daily temperature (*source* [50])

The same FE model conditions as explained in Sect. 3.2 was utilized, and the weather conditions of the simulation was set up by calibrating deck temperatures of sound parts based on the weather record from the closest weather station [50], approximately 15 km away from the bridge. The sunrise was 7:06 a.m. and sunset was 6:51 p.m. on that day, and the daily temperature is shown in Fig. 20. Based on the weather record, it was cloudy during the daytime and clear during the nighttime. Since the IRT data was collected at 10:30 PM, ΔT of simulation results at 10:30 p.m. were compared. In the delamination model of $40 \times 40 \times 0.1$ cm, the depths of delamination were changed every 1 cm from 3 to 6 cm, and the depths of $40 \times 40 \times 1$ cm model were simulated from 4 to 7 cm. Table 6 summarizes ΔT of IRT data and FE model simulations for each case.

In the case of $40 \times 40 \times 0.1$ cm delamination model, ΔT were −0.36 °C when the depth was 5 cm and −0.25 °C when the depth was 6 cm; therefore, the depth of the real delamination can be assumed between 5 and 6 cm if the thickness is 0.1 cm. On the other hand, ΔT of $40 \times 40 \times 1$ cm delamination model were −0.55 °C at 6 cm depth and −0.29 °C at 7 cm depth; thus, the depth of the real delamination can be assumed to be between 6 and 7 cm if the thickness is 1 cm or more. Since the thickness of the delamination is also unknown as mentioned above, the depth of the real delamination can be assumed to be between minimum and maximum depths from the two cases of FE modeling. Therefore, the

Table 6 ΔT of IRT data and FE model simulations for each case

10:30 PM	IRT	Thickness: 0.1 cm				Thickness: 1 cm			
Depth	Unknown	3 cm	4 cm	5 cm	6 cm	4 cm	5 cm	6 cm	7 cm
Del. (°C)	18.69	18.29	18.41	18.53	18.64	17.60	17.97	18.30	18.58
Sound (°C)	19.02	18.90	18.89	18.89	18.89	18.83	18.84	18.85	18.87
ΔT (°C)	−0.33	−0.61	−0.48	−0.36	−0.25	−1.23	−0.87	−0.55	−0.29

depth of the delamination indicated by IRT can be estimated to be 5–7 cm deep from the surface. This result matches the depth of the core sample that is approximately 6 cm from the surface. Thus, it can be concluded that this estimation method worked properly by incorporating IRT with FE modeling.

6 Conclusions

In this study, the effects of area, thickness and shape of delaminations on subsurface defect detectability by IRT is explored through FE modeling. The temperature difference between sound and delaminated areas, ΔT, is considered as the reference value to discuss its detectability by IRT since it is the most important factor for IRT to identify the existence of subsurface delaminations from thermal images. Regarding the effect of delamination thickness, it is shown that ΔT increases as the thickness of delamination increases; however, ΔT converges to a certain point of ΔT when the thickness of delamination becomes at least 1 cm. In terms of the effect of delamination area, it is found that as the area of delamination becomes larger, the effect on its detectability by IRT becomes bigger since the area of delamination strongly affects ΔT; however, if the area becomes more than 30×30 cm, ΔT converges to a certain value when the delamination area is approximately 40×40 cm. As for the shape of delamination, not only square shape of delaminations, but also rectangular and circular shapes of delaminations are modeled and analyzed. The results show that only rectangular-shaped delaminations which have 25% or lower ratios of shorter side length to longer side length generate distinctly smaller ΔT than the other delaminations which have the same area regardless of shape. Therefore, it can be assumed that if the aspect ratio (ratio of the length of the shorter side to the longer side of the delamination) is more than 25%, ΔT of any delaminations converges to ΔT of the same area of a square/circular-shaped delamination. Furthermore, it can also be concluded that if the aspect ratio is 25% or smaller, ΔT becomes smaller than the ΔT of the same area of a square/circular-shaped delamination, and it is getting smaller as the ratio becomes smaller. It should be noted that these results are determined by FE modeling which was validated with limited test specimens and experimental data, so more experimental data is desired to provide evident results.

Through the present study, a strong correlation was found between the size of delamination and the depth from the concrete surface in regard to ΔT. This led to an investigation of the possibility to overcome IRT's depth information limitation by estimating the depth of the delamination using IRT. In order to investigate the possibility whether or not IRT can provide information about the depth of delamination, IRT data from real bridge deck scanning was utilized. It was assumed that it was possible to estimate the depth of delamination by comparing ΔT from IRT data to ΔT at several depths obtained from FE model simulations. Since ΔT converges to a certain value which is approximately ΔT of $40 \times 40 \times 1$ cm of square, ΔT of the two sizes of delaminations were assumed to be minimum ΔT, which is ΔT of $40 \times 40 \times 0.1$ cm, and maximum ΔT, which is ΔT of $40 \times 40 \times 1$ cm. By comparing ΔT from IRT data to ΔT at several depths, the real delamination's depth from the surface can be assumed to be between 5 and 7 cm based on these two cases of FE model simulations. Since the depth is approximately 6 cm from the surface, it can be concluded that this estimation method worked properly to provide delamination depth information by incorporating IRT with FE modeling in this case study.

Acknowledgements This work was supported mainly by West Nippon Expressway Company Limited (NEXCO-West) and also by the Scientific and Technological Research Council of Turkey (TÜBİTAK) and National Science Foundation (NSF CMMI #1463493). The authors would like to express their sincere gratitude to Mr. Masato Matsumoto, Mr. Hiroyuki Kato, Mr. Katsuya Aoki and Mr. Kyle Ruske of NEXCO-West USA for their technical help with the project in Florida. The authors would also like to express sincere appreciation to Mr. Juan Cruz and our other research group members for their support with manufacturing test specimens and setting up equipment. Furthermore, the authors are also thankful to Andy Derewiany for editing the manuscript.

References

1. Hiasa, S., Birgul, R., Catbas, F.N.: Infrared thermography for civil structural assessment: demonstrations with laboratory and field studies. J. Civ. Struct. Heal. Monit. **6**, 619–636 (2016)
2. Kashif Ur Rehman, S., Ibrahim, Z., Memon, S.A., Jameel, M.: Nondestructive test methods for concrete bridges. A review. Constr. Build. Mater. **107**, 58–86 (2016)

3. Theodorakeas, P., Cheilakou, E., Ftikou, E., Koui, M.: Passive and active infrared thermography: an overview of applications for the inspection of mosaic structures. In: 33rd UIT (Italian Union Thermo-Fluid Dynamics Heat Transfer Conference 655 (2015)
4. Holst, G.C.: Common Sense Approach to Thermal Imaging. JCD Publishing, Winter Park (2000)
5. Tashan, J., Al-mahaidi, R., Mamkak, A.: Defect size measurement and far distance infrared detection in CFRP-concrete and CFRP-steel systems. Aust. J. Struct. Eng. **17** (2015). doi.10.1080/13287982.2015.1116177
6. Washer, G., Fenwick, R., Nelson, S., Rumbayan, R.: Guidelines for the thermographic inspection of concrete bridge components in shaded conditions. Transp. Res. Rec. J. Transp. Res. Board. **2360**, 13–20 (2013)
7. Huh, J., Tran, Q.H., Lee, J., Han, D., Ahn, J., Yim, S.: Experimental study on detection of deterioration in concrete using infrared thermography technique. Adv. Mater. Sci. Eng. **2016**, Article ID 1053856 (2016)
8. Cotič, P., Kolarič, D., Bosiljkov, V.B., Bosiljkov, V., Jagličić, Z.: Determination of the applicability and limits of void and delamination detection in concrete structures using infrared thermography. NDT E Int. **74**, 87–93 (2015)
9. FHWA: Highway bridges by deck structure type 2016. https://www.fhwa.dot.gov/bridge/nbi/no10/deck16.cfm
10. Hiasa, S.: Investigation of infrared thermography for subsurface damage detection of concrete structures. Electronic Theses and Dissertations Paper 5063 (2016). http://stars.library.ucf.edu/etd/5063
11. Hiasa, S., Catbas, F.N., Matsumoto, M., Mitani, K.: Considerations and issues in the utilization of infrared thermography for concrete bridge inspection at normal driving speeds. J. Bridg. Eng., ASCE (2017). doi:10.1061/(ASCE)BE.1943-5592.0001124
12. Hiasa, S., Catbas, F.N., Matsumoto, M., Mitani, K.: Monitoring concrete bridge decks using infrared thermography with high speed vehicles. Struct. Monit. Maint. Int. J. **3**, 277–296 (2016)
13. Khan, F., Bolhassani, M., Kontsos, A., Hamid, A., Bartoli, I.: Modeling and experimental implementation of infrared thermography on concrete masonry structures. Infrared Phys. Technol. **69**, 228–237 (2015)
14. McCann, D.M., Forde, M.C.: Review of NDT methods in the assessment of concrete and masonry structures. NDT E Int. **34**, 71–84 (2001)
15. Maldague, X.P.: V: introduction to NDT by active infrared thermography. Mater. Eval. **60**, 1060–1073 (2002)
16. Waugh, R.C.: Development of infrared techniques for practical defect identification in bonded joints. In: Development of Infrared Techniques for Practical Defect Identification in Bonded Joints, pp. 21–37. Springer International Publishing, Heidelberg (2016)
17. Sebesta, S., Saarenketo, T., Scullion, T.: Using Infrared and High-Speed Ground-Penetrating Radar for Uniformity Measurements on New HMA Layers. The National Academies Press, Washington, DC (2012)
18. Hiasa, S., Birgul, R., Catbas, F.N.: Investigation of effective utilization of infrared thermography (IRT) through advanced finite element modeling. Constr. Build. Mater. (2017). doi:10.1016/j.conbuildmat.2017.05.175
19. Vavilov, V.P.: Pulsed thermal NDT of materials: back to the basics. Nondestruct. Test. Eval. **22**, 177–197 (2007)
20. Washer, G., Fenwick, R., Bolleni, N.: Development of hand-held thermographic inspection technologies. Report No. OR10-007 (2009)
21. Washer, G., Fenwick, R., Bolleni, N.: Effects of solar loading on infrared imaging of subsurface features in concrete. J. Bridg. Eng. **15**, 384–390 (2010)
22. Gucunski, N., Nazarian, S., Yuan, D., Kutrubes, D.: Nondestructive testing to identify concrete bridge deck deterioration. Transportation Research Board, SHRP 2 Report S2-R06A-RR-1, Washington, DC (2013)
23. Yehia, S., Abudayyeh, O., Nabulsi, S., Abdelqader, I.: Detection of common defects in concrete bridge decks using nondestructive evaluation techniques. J. Bridg. Eng. **12**, 215–225 (2007)
24. Kee, S.-H., Oh, T., Popovics, J.S., Arndt, R.W., Zhu, J.: Nondestructive bridge deck testing with air-coupled impact-echo and infrared thermography. J. Bridg. Eng. **17**, 928–939 (2012)
25. Watase, A., Birgul, R., Hiasa, S., Matsumoto, M., Mitani, K., Catbas, F.N.: Practical identification of favorable time windows for infrared thermography for concrete bridge evaluation. Constr. Build. Mater. **101**, 1016–1030 (2015)
26. ASTM: Standard Test Method for Detecting Delaminations in Bridge Decks Using Infrared Thermography. ASTM International, West Conshohocken (2014)
27. Hashimoto, K., Akashi, Y.: Points to consider for photography by infrared cameras with different wavelength detection region. In: 65th JSCE Annual Meeting, p. VI-160. Japan Society of Civil Engineers (JSCE), Sapporo, Japan (2010)
28. FLIR: The Ultimate Infrared Handbook for R&D Professionals. FLIR AB (2013)
29. Nishikawa, T., Hirano, A., Kamada, E.: Experimental study on thermography method for external wall removement finished with ceramic tile. Arch. Inst. Jpn. **529**, 29–35 (2000)
30. Nakamura, S., Takaya, S., Maeda, Y., Yamamoto, T., Miyagawa, T.: Spalling time prediction by using infrared thermography. J. Jpn. Soc. Civ. Eng. Ser. E2 (Materials Concr. Struct.) **69**, 450–461 (2013)
31. Maierhofer, C., Brink, A., Ro, M., Wiggenhauser, H.: Quantitative impulse-thermography as non-destructive testing method in civil engineering—experimental results and numerical simulations. Constr. Build. Mater. **19**, 731–737 (2005)
32. Cheng, C.-C., Cheng, T., Chiang, C.: Defect detection of concrete structures using both infrared thermography and elastic waves. Autom. Constr. **18**, 87–92 (2008)
33. Abdel-qader, I., Yohali, S., Abudayyeh, O., Yehia, S.: Segmentation of thermal images for non-destructive evaluation of bridge decks. NDT E Int. **41**, 395–405 (2008)
34. Rumbayan, R., Washer, G.A.: Modeling of environmental effects on thermal detection of subsurface damage in concrete. Res. Nondestruct. Eval. **25**, 235–252 (2014)
35. Cannas, B., Carcangiu, S., Concu, G., Trulli, N.: Modeling of active infrared thermography for defect detection in concrete structures. In: COMSOL Conference 7 (2012)
36. Restrepo Girón, A.D., Loaiza Correa, H.: New 3D finite difference method for thermal contrast enhancement in slabs pulsed thermography inspection. J. Nondestruct. Eval. **33**(1), 62–73 (2013)
37. Krishnapillai, M., Jones, R., Marshall, I.H., Bannister, M., Rajic, N.: NDTE using pulse thermography: numerical modeling of composite subsurface defects. Compos. Struct. **75**, 241–249 (2006)
38. Vavilov, V.P., Burleigh, D.D., Klimov, A.G.: Advanced modeling of thermal NDT problems: from buried landmines to defects in composites. In: Maldague, X.P., Rozlosnik, A.E. (eds.) Thermosense XXIV, pp. 507–521. SPIE, Orlando (2002)
39. COMSOL: Heat Transfer Module User's Guide, Version 5.1 (2015)
40. Google: Google Maps. https://www.google.com/maps/
41. WeatherUnderground: Weather History for Orlando, FL [KFLORLAN179], http://www.wunderground.com/personal-weather-station/dashboard?ID=KFLORLAN179#history/tdata/s20151219/e20151219/mdaily
42. Kumar, S., Mullick, S.C.: Wind heat transfer coefficient in solar collectors in outdoor conditions. Sol. Energy **84**, 956–963 (2010)
43. Sharples, S., Charlesworth, P.S.: Full-scale measurements of wind-induced convective heat transfer from a roof-mounted flat plate solar collector. Sol. Energy **62**, 69–77 (1998)

44. Kumar, S., Sharma, V.B., Kandpal, T.C., Mullick, S.C.: Wind induced heat losses from outer cover of solar collectors. Renew. Energy **10**, 613–616 (1997)
45. Meola, C.: A new approach for estimation of defects detection with infrared thermography. Mater. Lett. **61**, 747–750 (2007)
46. Farrag, S., Yehia, S., Qaddoumi, N.: Investigation of mix-variation effect on defect-detection ability using infrared thermography as a nondestructive evaluation technique. J. Bridg. Eng. **21**, 4015055 (2015)
47. Clark, M., McCann, D., Forde, M.: Application of infrared thermography to the non-destructive testing of concrete and masonry bridges. NDT E Int. **36**, 265–275 (2003)
48. Oh, T., Kee, S., Arndt, R.W., Popovics, J.S., Asce, M., Zhu, J.: Comparison of NDT methods for assessment of a concrete bridge deck. J. Eng. Mech. **139**, 305–314 (2013)
49. Matsumoto, M., Mitani, K., Catbas, F.N.: Bridge assessment methods using image processing and infrared thermography. In: 28th US–Japan Bridge Engineering Workshop (2012)
50. WeatherUnderground: Hourly Weather History & Observations. https://www.wunderground.com/history/airport/KHEF/2014/10/2/DailyHistory.html?req_city=Haymarket&req_state=VA&req_statename=&reqdb.zip=20168&reqdb.magic=1&reqdb.wmo=99999&MR=1